

Provided for non-commercial research and education use.  
Not for reproduction, distribution or commercial use.



(This is a sample cover image for this issue. The actual cover is not yet available at this time.)

**This article appeared in a journal published by Elsevier. The attached copy is furnished to the author for internal non-commercial research and education use, including for instruction at the authors institution and sharing with colleagues.**

**Other uses, including reproduction and distribution, or selling or licensing copies, or posting to personal, institutional or third party websites are prohibited.**

**In most cases authors are permitted to post their version of the article (e.g. in Word or Tex form) to their personal website or institutional repository. Authors requiring further information regarding Elsevier's archiving and manuscript policies are encouraged to visit:**

**<http://www.elsevier.com/copyright>**



Contents lists available at SciVerse ScienceDirect

## Remote Sensing of Environment

journal homepage: [www.elsevier.com/locate/rse](http://www.elsevier.com/locate/rse)

# Advantages and limitations of ocean color remote sensing in CDOM-dominated, mineral-rich coastal and estuarine waters

Dirk A. Aurin<sup>\*</sup>, Heidi M. Dierssen

University of Connecticut, Department of Marine Sciences, Groton, CT, USA

## ARTICLE INFO

## Article history:

Received 1 September 2011  
 Received in revised form 31 May 2012  
 Accepted 10 July 2012  
 Available online xxxx

## Keywords:

Ocean color  
 Remote sensing  
 Semi-analytical algorithm development  
 Regional optimization

## ABSTRACT

Current operational approaches to ocean color remote sensing tend to be least accurate in coastal regions with waters rich in terrigenous material. Semi-analytical models can be used to retrieve the absorption and backscattering properties of dissolved and suspended materials unique to these environments, and subsequently biogeochemical parameters such as total suspended material (TSM) and chlorophyll (Chl). In this study, optical data collected over several years are used to select and optimize a semi-analytical ocean color algorithm for the dynamic and optically complex Long Island Sound estuary. The most successful algorithm requires a red reflectance channel between 600 and 650 nm, which is not included in many current ocean color sensors, but is essential in highly scattering waters. Regional optimization including the use of a dynamic, spectrally variable  $f/Q$ , a value related to the bidirectional reflectance distribution function (BRDF), results in an approximately five-fold decrease in retrieval bias in highly backscattering, sediment-laden waters near river outflows. Retrievals of dissolved and particulate spectral absorption, backscattering, dissolved and detrital absorption coefficients and total suspended matter obtained from the optimized algorithm agree well with field observations ( $r^2 \geq 0.90$ ). These parameters are useful for assessing riverine discharge, mixing and residence times of surface waters, as well as assessing the turbidity and light penetration in this estuary. Estimation of Chl remains challenging ( $r^2 = 0.59$ ) due to the stepwise nature of the algorithm and the relatively high proportion of dissolved and non-algal constituents masking phytoplankton absorption (generally <20% of total absorption at 440 nm). Moreover, diverse phytoplankton assemblages throughout the region create variability between spectral absorption and chlorophyll and highlight the benefits of increased spectral resolution of ocean color satellites going forward.

© 2012 Elsevier Inc. All rights reserved.

## 1. Introduction and background

Ocean color imagery collected over the past three decades from numerous orbital platforms has the potential for providing long-term, synoptic retrievals of bio-optical properties in the world's oceans (McClain, 2009). However, satellite ocean color imagery is generally underutilized or improperly interpreted in coastal and estuarine systems largely because standard approaches for retrieving water column properties from space cannot accommodate the optical complexity deriving from riverine delivery of dissolved and sedimentary material. Both the sensors and algorithms used for routine ocean remote sensing are optimized for open ocean conditions (Dierssen, 2010). Improving retrievals of water borne constituents in other environments including near shore and estuarine systems requires optimization of algorithms using regional *in situ* measurements of optical and biogeochemical water properties.

Historically, many ocean color algorithms have been developed to retrieve inherent optical properties (IOPs; properties that depend

on the optically significant materials in the water column including phytoplankton and sediments) and/or biogeochemical properties (e.g., chlorophyll-a concentration Chl, total suspended material TSM, and chromophoric dissolved organic material CDOM) based on direct empirical relationships with the remote sensing reflectance,  $R_{rs}(\lambda)$ , or ratios of  $R_{rs}$  at various wavelengths (see Table 1 for definitions). In recent years, many new semi-analytical ocean color algorithms (SAAs) (Arnone et al., 2006) and other inversion methods such as neural networks (e.g. Doerffer & Schiller, 2007; Ioannou et al., 2011) have been developed to include retrievals of IOPs in optically complex coastal and estuarine systems where global empirical approaches often fail. In this study, we evaluate remote sensing algorithms in Long Island Sound (LIS; Fig. 1) with an eye to evaluating the requirements needed to most accurately retrieve optical and biogeochemical properties in complex estuarine waters and the limitations of semi-analytical methods for retrieving phytoplankton properties in a taxonomically diverse environment dominated by dissolved and non-algal absorption.

### 1.1. Optical models used in algorithm development

The SAAs studied here rely on the principle that the spectral remote sensing reflectance immediately below the sea surface ( $r_{rs}(\lambda)$ )

<sup>\*</sup> Corresponding author at: Science Systems and Applications Inc., NASA Goddard Space Flight Center, Mail Code 616, Bldg 22, Rm 248, Greenbelt, MD 20771, USA. Tel.: +1 301 286 2742.

E-mail address: [dirk.a.aurin@nasa.gov](mailto:dirk.a.aurin@nasa.gov) (D.A. Aurin).

**Table 1**  
Summary of abbreviations and acronyms.

	Units	Definition
$a(\lambda)$	$m^{-1}$	Total absorption coefficient
$a_g(\lambda)$	$m^{-1}$	CDOM (or gelbstoff) absorption coefficient
$a_d(\lambda)$	$m^{-1}$	NAP (or detrital) absorption coefficient
$a_p(\lambda)$	$m^{-1}$	Particulate absorption coefficient
$a_\phi(\lambda)$	$m^{-1}$	Phytoplankton absorption coefficient
$a_\phi^*(\lambda)$	$m^2 (\text{mg Chl-a})^{-1}$	Chlorophyll-specific phytoplankton absorption coefficient
$a_w(\lambda, T, S)$	$m^{-1}$	Pure seawater absorption coefficient
$b(\lambda), b_p(\lambda)$	$m^{-1}$	Total, particulate scattering coefficient
$b_b(\lambda), b_{bp}(\lambda)$	$m^{-1}$	Total, particulate backscattering coefficient
$c(\lambda), c_p(\lambda)$	$m^{-1}$	Total, particulate attenuation coefficient
$E_d(\lambda)$	$W m^{-2} nm^{-1}$	Downwelling irradiance
$g_0, g_1, f/Q, BRDF$	$sr^{-1}$	Factors relating $r_{rs}$ to $a$ and $b_b$
$L_u(\lambda, z), L_w(\lambda)$	$W m^{-2} nm^{-1} sr^{-1}$	Upwelling, water-leaving radiance
$R_{rs}(\lambda), r_{rs}(\lambda)$	$sr^{-1}$	Above, below surface remote sensing reflectance
$S_g$	$nm^{-1}$	Exponential slope of $a_g$
$S_d$	$nm^{-1}$	Exponential slope of $a_d$
$Y$		Power-law slope of $b_{bp}$
$\zeta$		Spectral shape parameter for $a_\phi$
$\xi$		Spectral shape parameter for $a_{dg}$
$\lambda, \lambda_0$	nm	Wavelength, reference wavelength
BRDF		Bi-directional Reflectance Distribution Function
CDOM		Colored Dissolved Organic Material
Chl	$mg m^{-3}$	Chlorophyll-a concentration
CTR		Connecticut River
NAP		Non-algal material
PSD	particles $ml^{-1} \mu m^{-1}$	Particle size distribution
SAA		Semi-analytical ocean color algorithm
TSM	$mg L^{-1}$	Total suspended material

can be modeled as a polynomial function of the spectral backscattering and absorption coefficients (Gordon et al., 1975, 1988; Morel & Prieur, 1977):

$$r_{rs}(\lambda) = \frac{L_u(\lambda, 0^-)}{E_d(\lambda, 0^-)} = g_0 u(\lambda) + g_1 u(\lambda)^2, \quad (1)$$

where

$$u(\lambda) = \frac{b_b(\lambda)}{a(\lambda) + b_b(\lambda)}. \quad (2)$$

$L_u$  and  $E_d$  are the spectral upwelling radiance and downwelling irradiance, respectively, just below the surface (depth = 0<sup>-</sup>). The below surface  $r_{rs}(\lambda)$  is calculated from above surface  $R_{rs}(\lambda)$  measurements following Gordon et al. (1988) and Mobley (1994) as described

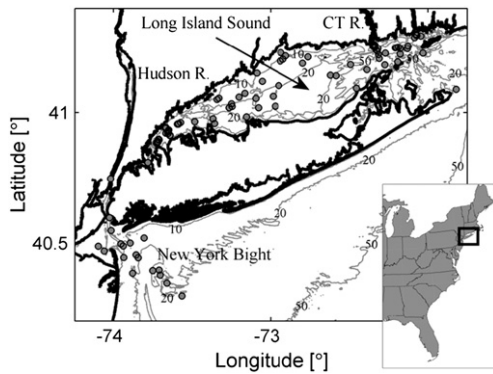


**Fig. 1.** Long Island Sound is a relatively shallow estuary (bathymetric contours shown in gray) with strong tidal and sub-tidal exchange at its eastern end. The Connecticut (CT) River delivers the majority of the fresh water to the estuary, although the Hudson River impacts the optical properties in western LIS through exchanges at the western end (Aurin et al., 2010). Stations sampled for algorithm optimization (dots) were widely distributed across the region.

in Lee et al. (1999) Appendix A, and Lee et al. (2002) Section 2.B. The values  $g_0$  and  $g_1$  are empirically derived parameters related to the  $f/Q$  term (see Section 1.1.1) often cited in the literature (i.e.  $r_{rs}(\lambda) = g_0 u(\lambda) + g_1 u(\lambda)^2 = f/Q^* u(\lambda)$ ;  $f/Q = g_0 + g_1 u(\lambda)$ ) encompassing the directional nature of the upwelling light field ( $Q$ ), and  $f$ , the relationship between the magnitude of the irradiance reflectance and the IOPs. Within the typical remote sensing geometry (see Section 1.1.1),  $f/Q$  is generally assumed to be fairly constant, but in fact, extensive work has shown how  $f/Q$  depends on solar zenith angle, viewing angle, aerosol optical thickness of the atmosphere, wind speed, and the magnitudes of the IOPs themselves (Lee et al., 2011; Morel & Gentili, 1991, 1993; Morel & Gentili, 1996; Morel et al., 2002; Park & Ruddick, 2005).

The total absorption coefficient can be linearly separated into contributions by seawater ( $a_w$ ) and particulate and dissolved absorption ( $a_{pg}$ ). The latter can be further separated into absorption contributions by phytoplankton ( $a_\phi$ ), non-algal particulates ( $a_d$ ), and CDOM ( $a_g$ ) (Eq. 3). The backscattering coefficient comprises contributions by particles and seawater (backscattering by dissolved material is considered negligible):

$$a(\lambda) = a_\phi(\lambda) + a_d(\lambda) + a_g(\lambda) + a_w(\lambda); \quad b_b(\lambda) = b_{bp}(\lambda) + b_{bw}(\lambda). \quad (3)$$

Absorption and backscattering by seawater are well established (Buiteveld et al., 1994; Pope & Fry, 1997; Smith & Baker, 1981), and the dissolved and non-algal absorption are generally modeled with an exponentially decaying function with increasing wavelength. Because of their similarity in spectral shape, absorption by CDOM is difficult to distinguish from absorption by NAP in retrievals, and ocean color algorithms generally retrieve only their sum,  $a_{dg}(\lambda)$  (Arnone et al., 2006) :

$$a_{dg}(\lambda) = a_{dg}(\lambda_0) e^{-S_{dg}(\lambda - \lambda_0)} \quad (4)$$

where  $S_{dg}$  is the spectral slope parameter and  $\lambda_0$  is a reference wavelength.

The particulate backscattering coefficient  $b_{bp}(\lambda)$  is modeled using the power-law form commonly found in SAAs (Carder et al., 1999; Lee et al., 2002; Roesler & Boss, 2002):

$$b_{bp}(\lambda) = b_{bp}(\lambda_0) \left( \frac{\lambda_0}{\lambda} \right)^Y, \quad (5)$$

where  $Y$  describes the spectral shape, despite concerns that the shape of backscattering is not entirely independent of absorption, and anomalous dispersion affects the shape of backscattering throughout the visible, but most notably near the red absorption peak (Zaneveld & Kitchen, 1995).

Incorporation of the IOP spectral models (Eqs. (3)–(5)) into the generic form of the remote sensing reflectance model (Eqs. (1) and (2)) yields the formulation of the SAA convenient for remote sensing:

$$r_{rs}(\lambda) = \sum_{i=1,2} g_{i-1} \left( \frac{b_{bp}(\lambda_0) \left( \frac{\lambda_0}{\lambda} \right)^Y + b_{bw}(\lambda)}{a_\phi(\lambda) + a_{dg}(\lambda) e^{-S_{dg}(\lambda - \lambda_0)} + a_w(\lambda) + b_{bp}(\lambda_0) \left( \frac{\lambda_0}{\lambda} \right)^Y + b_{bw}(\lambda)} \right)^i \quad (6)$$

### 1.1.1. Variability in the BRDF

A large body of work exists in the literature describing the BRDF as a function of the IOPs (namely absorption and backscattering coefficients and the volume scattering function, VSF), the solar zenith angle, sensor viewing angles, wind speed, and aerosol optical thickness (Gordon et al., 1988; Lee et al., 1999; Morel & Gentili, 1991, 1993; Morel & Gentili, 1996; Morel et al., 2002; Preisendorfer, 1961, 1965). In general, they agree that within the remote sensing domain (i.e. depending on the particular study, solar zenith angle  $\leq \sim 60^\circ$ , sensor viewing angle  $\leq \sim 40^\circ$ , aerosol optical thickness  $\leq \sim 0.4$ , wind

speed  $< \sim 10 \text{ m s}^{-1}$ , and assumptions consistent with quasi-single-scattering theory (Gordon et al., 1975))  $f/Q$  varies by  $< 10\%$ , and has only a weak dependence on wavelength. The  $g_0$  and  $g_1$  values reported in Gordon et al. (1988) and Lee et al. (1999) were derived empirically after performing numerical radiative transfer models on simulated data. Without detailed *a priori* knowledge of the volume scattering function of the aggregate particles in the water column (which cannot be measured remotely),  $g_0$  and  $g_1$  (and therefore  $f/Q$ ) cannot be determined analytically. The parameter  $f/Q$  was historically modeled and parameterized using the Case 1 assumption that volume scattering and absorption properties could be estimated from Chl. More recently, modeling studies have refined estimations of  $f/Q$  to extend Eq. (1) to Case 2 waters (Gleason et al., 2012; Hlaing et al., 2012; Lee et al., 2011; Park & Ruddick, 2005) by incorporating variability in solar and viewing geometry and allowing estimates of the volume scattering function (and therefore  $f/Q$ ) to vary somewhat with changes in optical water type, but except in the case of Hlaing et al. (2012), spectral dependence was not included. These corrections to the BRDF generally reduce error in  $f/Q$  for “typical” Case 1 and Case 2 waters, but they are generally not adaptive to large changes in the particle phase function nor parameterized for extremely turbid waters such as those occasionally encountered in LIS. Like earlier approaches, the model of Hlaing et al. (2012) is based upon a simulated IOP dataset, but in this case extending to the dynamic range of our field data (Aurin et al., 2010). Furthermore, it was validated using reflectances measured in LIS, and it retains spectral dependence which we will show to be a factor at some highly turbid river plume stations. It differs only slightly in its formulation, using a third-degree polynomial where we use a quadratic expression in Eq. (1), but the higher degree terms have very little effect on algorithm performance in our region as we will show in Section 4. We therefore investigate the performance of the Hlaing et al. (2012) BRDF correction approach (hereafter referred to as the CCNY model or correction) with our field data.

In a recent study by Brando et al. (2012) based on field data collected in the optically complex waters off Australia as well as simulated data, the authors demonstrated that the BRDF parameterization had a significant impact on the ability of a linear matrix inversion (LMI)-type algorithm to make accurate retrievals of IOPs and Chl, and suggested a future optimization including an adaptive selection process. They found that use of the values from Gordon et al. (1988) instead of those from Lee et al. (1999) reduced the number of possible retrievals to less than half of their data set, while substantially reducing the accuracy of the remaining retrievals. As shown below, the choice of  $f/Q$  was found to be critical for remote sensing in turbid river plumes.

### 1.2. Spectral availability of satellite ocean color data

The current suite of global ocean color sensors have multiple spectral bands spanning the visible wavelengths (VIS, 400–700 nm, Fig. 2). These bands are not spread uniformly across the visible spectrum, but have been selected to correspond to reflectance characteristics of open ocean waters, particularly those related to phytoplankton pigment absorption features. Three bands are generally found in “blue” (near 412, 443, and 490 nm), 1–2 bands in “green” (510, 555 nm), and 1–2 channels in the “red” (670, 680 nm). In fact, a full third of the visible spectrum (555–670 nm) is not routinely sampled by most current sensors with enough sensitivity for ocean color remote sensing. Exceptions to this trend include the current European Space Agency (ESA) MERIS sensor and the planned (2013) ESA OLCI sensor on Sentinel-3, each of which includes a 620 nm ocean band. There is also a 645 nm band on the MODIS sensors (Aqua and Terra), but this band was not designed for ocean color analysis. It has a very broad spectral response ( $\sim 50$  nm) and a low signal to noise ratio (SNR) geared for land-based remote sensing; the on-orbit SNR for the 645 nm band is  $\sim 200$  (Xiong et al., 2010) versus  $\sim 2000$

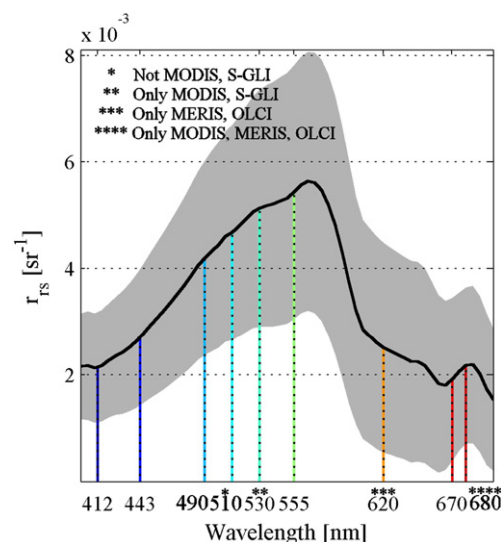


**Fig. 2.** Spectral locations (approximate band centers in color; available online) of ocean color bands for the SeaWiFS, MODIS (Aqua and Terra), MERIS, OLCI, S-GLI and VIIRS (NPP and NPOES) sensors (NRC, 2011) overlaid on the median remote sensing reflectance spectrum (black line) and standard deviation (shaded region) for LIS. With the exception of the MERIS and OLCI sensors, a notable gap in coverage exists between 555 nm and 670 nm due to a lack of prominent absorption features in this region of the spectrum. MODIS instruments have a wide-band, low SNR 645 nm band designed for land use which may be applied to ocean color under certain circumstances (see text). (For interpretation of the references to color in this figure legend, the reader is referred to the web version of this article.)

for ocean color bands. This limits the use of this band to only the most turbid coastal waters where the particulate backscattering coefficient in the red is high enough to overcome the strong absorption coefficient of water, leading to a sufficient water leaving radiance signal in the 645 nm band (e.g. Miller & McKee, 2004). While such conditions can be expected in many areas within LIS – particularly during periods of high river flow – it remains unknown how broadly this band can be applied across the region.

The history of band selection was based in part on the concept of a spectral “hinge point” where waters turn from blue to green with the addition of chlorophyll-a (Gordon & Morel, 1983). The band near 440 nm coincides with the strongest chlorophyll-a absorption peak, while absorption by the phycobiliproteins found in cryptomonads and cyanobacteria is centered near the 490 and 510 nm bands. These longer, blue-green wavebands are also critical to the detection of algae in waters where absorption by chromophoric dissolved material (CDOM) and non-algal particulates (NAP) is significant and may obscure chlorophyll absorption features near 443 nm. The 412 nm band is associated with absorption by CDOM and NAP which decrease exponentially with increasing wavelength. The green band near 555 nm generally coincides with the peak in spectral reflectance when chlorophyll concentrations are greater than  $\sim 5 \text{ mg m}^{-3}$ . When intense phytoplankton blooms or “red tides” are present at the sea surface, the spectral peak can be shifted towards 590 nm (Dierssen et al., 2006; Ryan et al., 2005). The red channels are grouped at the far end of the visible spectrum (Fig. 2) in order to capture the *in vivo* chlorophyll absorption peak around 676 nm and the chlorophyll fluorescence signature at 685 nm (Behrenfeld et al., 2009). However, even the fluorescence channels can be largely dominated by scattering or “red-edge reflectance” during intense algal blooms (Dierssen et al., 2006; Gilerson et al., 2008).

Band selection has also been based on identifying the minimum number of bands required to capture the natural variability in the reflectance signature, but this approach yields different spectral locations and numbers of wavebands depending on the optical water types used for optimization (e.g. Lee et al., 2007; Mueller, 1976; Sathyendranath et al., 1993).



The frequent lack of a band between 555 and 670 nm is in large part due to the lack of any relevant absorption or fluorescence features in this part of the spectrum besides water absorption itself. While the absorption spectrum of seawater is slightly dependent on temperature and salinity (Sullivan et al., 2006), the spectral shape rises abruptly at 600 nm and increases into the near infrared. Because water absorption is so much higher than any other natural constituent of seawater (e.g., phytoplankton, CDOM, NAP) in this red part of the spectrum, the total absorption characteristics are known *a priori* and can be attributed almost solely to seawater. We saw in the previous section that remote sensing reflectance is roughly proportional to the amount of backscattered light and inversely proportional to absorbed light. Therefore, knowledge of the total absorption in this red portion of the spectrum, rather than unnecessary, can be extremely useful for remote sensing applications in order to separate the spectral influence of constituent backscattering from absorption on the reflected light (Lee & Carder, 2002).

### 1.3. Long Island Sound

Prior to the 2010 study by Aurin et al. (2010), very little research had been conducted in LIS focusing on optical characterization and ocean color remote sensing. A brief summary of this research was presented by Aurin et al. (2010) who pointed out that prior investigations tended to be highly localized, did not include a comprehensive suite of optical data, nor address broader trends across the region. Regional optimization of ocean color algorithms typically requires extensive field sampling to characterize variability in the magnitude and spectral quality of optical properties. For example, Blondeau-Patissier et al. (2009) showed that for coastal waters sampled in northeastern Australia, diversity in the IOPs deriving from changes in location and seasonal forcing (i.e., wet- versus dry-season) lead to multiple optical domains within the region. Their study exemplified how highly dynamic regions may not be well suited to a single algorithm parameterization for all sub-regions and/or times of year. Similarly, multiple bio-optical water types were found in the optically complex waters of Tokyo Bay and the Santa Barbara Channel (Chang et al., 2007; Feng et al., 2005). In the latter study, it was shown that the nature of bio-optical water types was a function of the particle composition during various times of year, which varied from minerogenic to phytoplankton dominated particles. In contrast, Aurin et al. (2010) found that in LIS, while some sub-regions were characterized by phytoplankton-dominated particles and others by minerogenic particles, and while variability in the magnitudes of IOPs was very high, the spectral quality of IOPs did not vary significantly from one region or season to another.

LIS, an exceptionally turbid and productive estuary, is an ideal region to address remote sensing of optically complex waters. First, it has high variability in optical and biogeochemical properties and magnitudes that far surpass those found in most coastal waters (e.g.,  $0.07 < a_p(440) < 1.63 \text{ m}^{-1}$ ,  $0.006 < b_{bp}(660) < 0.124 \text{ m}^{-1}$ , and  $0.7 < \text{Chl} < 80.6 \text{ mg m}^{-3}$ ) (Aurin et al., 2010). The two largest sources of fresh water (i.e., the Hudson and Connecticut Rivers; Fig. 1) drive much of the variability in CDOM and NAP absorption ( $0.30 \pm 0.10 \text{ m}^{-1}$  (median  $\pm$  std) and  $0.115 \pm 0.107 \text{ m}^{-1}$ , respectively at 440 nm) and particle backscattering ( $0.019 \pm 0.020 \text{ m}^{-1}$  at 660 nm) within LIS, and represent one extreme optical endmember for the region. Reflectance and absorption spectra measured throughout the major basins of the estuary can be classified as either phytoplankton or sediment dominated, similar to those reported in Morel and Prieur (1977) and elsewhere, although Aurin et al. (2010) showed (their Fig. 9) that CDOM absorption at 440 nm was typically dominant ( $70\% \pm 13\%$  of  $a_{pg}(440)$ ) compared to phytoplankton ( $12\% \pm 8\%$ ) or NAP ( $19\% \pm 10\%$ ) absorption at 440 nm.

Compared to other coastal waters that have multiple bio-optical water types, ocean color parameters in LIS describing the spectral shapes of absorption and scattering (e.g.,  $Y$ ,  $S_g$ ,  $S_d$ , and  $\gamma$ ; see Table 1 and Sections 1.1 and 3 for definitions) are not significantly

different across the region, or between seasons (Aurin et al., 2010). This may be due to the homogenizing influence of vigorous tidal and sub-tidal flow in the estuary mixing extremely turbid, CDOM-rich waters found in river plumes with relatively clear waters entering the estuary from the North Atlantic, or due to relatively homogeneous dissolved and terrigenous material deriving from the surrounding watershed. Uniformity in these properties means that algorithms for remote sensing in LIS should only require a single, regional parameterization, thus considerably simplifying and expediting the retrieval of the surface water properties from remote sensing imagery.

## 2. Methodology

Four prominent SAAs and one variant are tested in this study for their accuracy in retrieving IOPs including  $a_{pg}(\lambda)$ ,  $a_c(\lambda)$ ,  $a_{dg}(\lambda)$ , and  $b_b(\lambda)$  using metrics found in the IOCCG Report 5 (Arnone et al., 2006). Based on their relative retrieval performance using *in situ* data collected across the region from 2004 to 2011, the top performing SAA is empirically, regionally optimized. Sensitivity to tuning parameters is identified in order to both improve performance of the regional algorithm for LIS and to contribute to ocean color algorithm development going forward. Methods for retrieving biogeochemical properties including total suspended material (TSM) and chlorophyll concentration (Chl) from IOP retrievals are also developed. In selecting algorithms for tuning, we limit our investigation to wave bands available on the MODIS Aqua and Terra satellite sensors, but modification for other ocean color sensors (e.g., VIIRS, MERIS or SeaWiFS) would be trivial.

### 2.1. Field sampling

Field measurements and discrete sampling for this study comprise hyperspectral  $R_{rs}(\lambda)$ , spectral and hyperspectral IOPs, Chl, high performance liquid chromatography (HPLC), particle size distribution (PSD), TSM and ancillary data collected at 158 stations in Long Island Sound and nearby waters (Fig. 1) during twelve cruises between May 2004 and December 2007 (Aurin et al., 2010). TSM and  $R_{rs}(\lambda)$  were collected at an additional 8 ELIS stations in September 2011. The dissolved absorption coefficient,  $a_g$ , the total non-water absorption coefficient ( $a_{pg} = a - a_w$ ), the total non-water attenuation coefficient,  $c_{pg}$ , and the particulate backscattering coefficient,  $b_{bp}$ , were measured with a profiling platform. Scattering ( $b_{pg}$ ) was calculated by subtracting  $a_{pg}$  from  $c_{pg}$ . Spectral whole and 0.2  $\mu\text{m}$  filtered absorption and attenuation were measured with the ac-9 or ac-S (WET Labs) instruments. The backscattering coefficient was most frequently measured with the BBFL2 or BB3 (WET Labs) instruments, although limited multispectral observations were made using the Hydrosat-6 (Hobilabs). Temperature, conductivity and pressure were measured using a CTD (SBE25 or SBE49, Seabird). Optical profile data were binned to 0.5 m. Weighted surface average values of IOPs were estimated following Zaneveld et al. (2005) using the radiative transfer software Hydrolight (Sequoia Scientific) to model the radiant light field.

Particle size distribution was measured using a LISST-100X (Sequoia Scientific) and processed to particle volume concentration using the software provided by Sequoia Scientific. Discrete seawater samples were collected at each station at one or more depths and filtered onto Whatman GFF (nominal pore size 0.7  $\mu\text{m}$ ) filters. Frozen samples were shipped to the University of Maryland's Horn Point Laboratory for HPLC analysis of pigments including Chl (Hooker et al., 2005; Van Heukelman & Thomas, 2001). Phytoplankton chemotaxonomic groupings were determined through analysis of HPLC pigment data using CHEMTAX v2 software (Wright & Jeffrey, 2006) in conjunction with pigment inversion ratios determined through field sampling in LIS by the Connecticut Department of Environmental

Protection (Li et al., 2004). At selected stations, the particulate, phytoplankton, non-algal particulate, and minerogenic absorption coefficients ( $a_p(\lambda)$ ,  $a_{\phi}(\lambda)$ ,  $a_d(\lambda)$ ,  $a_{min}(\lambda)$ ) were measured in a Cary 3E (Varian Inc.) or U-3010 (Hitachi Inc.) dual-beam spectrophotometer following NASA protocols (Bowers et al., 1996; Fargion & Mueller, 2000; Werdell & Roesler, 2003). Spectrophotometer data and data from WET Labs “ac” instruments which were not in mutual agreement (four stations) were eliminated from the dataset. TSM concentration was determined gravimetrically at selected stations during summertime cruises in 2005, 2006 and 2011 following the procedures outlined in NASA protocols (Hooker et al., 1995).

Hyperspectral (325 nm–1075 nm, 1 nm resolution) surface reflectance measurements were taken above the sea-surface with a Fieldspec radiometer (Analytical Spectral Devices) and processed to remote sensing reflectance  $R_{rs}$  following Gould et al. (2001) parameterized for the coastal zone. This approach employs *in situ* measurements of absorption and the spectral shape of scattering and NIR reflectance to improve upon the skylight correction of above-surface reflectance measurements, particularly in highly turbid waters. Also,  $R_{rs}$  was estimated using Satlantic's Hyperpro (350 nm–800 nm, ~3 nm resolution) or HTSRB (350 nm–800 nm, 1 nm resolution) instruments. Further details regarding data collection, processing (including corrections and calibration information), and quality assurance can be found in Aurin et al. (2010).

Stations were selected for use in algorithm tuning on the basis of the quality of optical closure, which is the agreement between the light field modeled by numerical radiative transfer approximation given  $a_{pg}(\lambda, z)$ ,  $b_b(\lambda, z)$ ,  $b(\lambda, z)$  (where  $z$  is depth) and ancillary observations measured in the field (Hydrolight, (Mobley, 1995)) and the light field measured *in situ*. To avoid possible measurement errors in our tuning dataset, only stations with optimal optical closure (i.e., rank 1, see Eq. 4 in Aurin et al. (2010)) were used in algorithm tuning. Therefore, in addition to mutually consistent absorption coefficients between the spectrophotometer and WET Labs “ac” measurements, we also retain only stations with mutually consistent  $R_{rs}$  and IOPs. Metrics used to evaluate algorithm performance in retrieving surface properties were the same as

those used in the fifth report of the International Ocean-Colour Coordinating Group, and included the regression coefficient  $r^2$ , percent difference (PD), root mean square error (RMSE), and bias. In cases where data had an approximately log-normal distribution (i.e., for Chl or waveband independent IOPs, as opposed to TSM and band-specific IOP retrievals), data were arranged in log space prior to calculating performance metrics (Maritorena et al., 2006). In addition, linear regression analysis of the measured and modeled IOPs (Type II, (Laws, 1997)) was evaluated for similarity of the regression slope to 1.0 and the intercept to 0.

### 3. Algorithm selection and tuning

#### 3.1. Semi-analytical algorithm performance

Optical properties measured in LIS (i.e.,  $a_{pg}$ ,  $a_{\phi}$ ,  $a_{dg}$ , and  $b_b$  at 412, 440, 488, 510, 532, 555, and 650 nm) were compared with those retrieved using five semi-analytical algorithms applied to *in situ* reflectance data: C99 (Carder et al., 1999, 2006), LMI (Boss & Roesler, 2006; Roesler & Perry, 1995; Wang et al., 2005), GSM01 (Garver & Siegel, 1997; Maritorena & Siegel, 2006; Maritorena et al., 2002), and QAA (Lee & Carder, 2004; Lee et al., 2002, 2006, 2010) referenced to 555 nm (QAA555) or 640 nm (QAA640). Fig. 3 shows that for the principal retrieval parameters  $a_{pg}(\lambda)$  and  $b_b(\lambda)$  the QAA640 outperformed others in nearly all metrics. In addition to more accurate retrievals in LIS prior to regional tuning, the QAA has the advantage that its stepwise nature simplifies independent parameter tuning compared with GSM01 or neural network approaches, in which optimization must be done for all parameters simultaneously. The QAA640 was therefore selected as the foundational algorithm for this region.

Briefly, the QAA640 takes advantage of empirical methods for deriving total absorption at a reference wavelength ( $a(\lambda_0)$ , where  $\lambda_0$  is 640 nm) using  $r_{rs}(\lambda_0)$  and  $a(\lambda_0)$ , the positive root of the quadratic Eq. (1) is solved to get  $u(\lambda_0)$ , and Eqs. (1) and

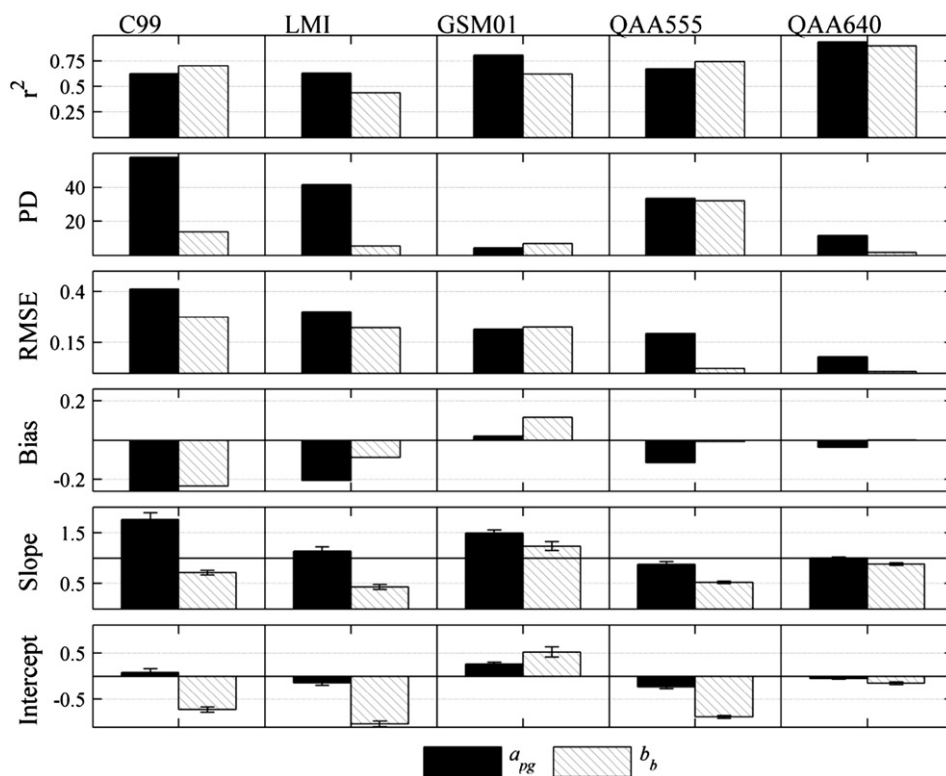


Fig. 3. Algorithm performance metrics (y-axes) prior to optimization for retrieving  $a_{pg}$  and  $b_b$  from *in situ*  $R_{rs}(\lambda)$  in LIS using five semi-analytical algorithms published in Report 5 of the International Ocean-Colour Coordinating Group (Arnone et al., 2006).

(2) are inverted to calculate the backscattering coefficient at the reference wavelength:

$$b_b(\lambda_0) = \frac{u(\lambda_0)a(\lambda_0)}{1-u(\lambda_0)} \quad (7)$$

The spectral slope of particulate backscattering,  $Y$ , is then estimated empirically using  $r_{rs}$  band ratios. Backscattering by seawater at the reference waveband ( $b_{bw}(\lambda_0)$ ) is subtracted to get  $b_{bp}(\lambda_0)$ , which is then expanded spectrally with  $Y$  and Eq. (5) to derive the fully spectral backscattering coefficient,  $b_{bp}(\lambda)$ . Next,  $b_{bw}(\lambda)$  is added back to  $b_{bp}(\lambda)$  yielding the total spectral backscattering coefficient,  $b_b(\lambda)$ , which is used to calculate the full spectral absorption coefficient analytically by inversion of Eq. (2):

$$a(\lambda) = \frac{(1-u(\lambda))b_b(\lambda)}{u(\lambda)} \quad (8)$$

The final steps of the QAA involve separating retrievals of total absorption into constituent components  $a_\phi$  and  $a_{dg}$ . The approach of the QAA to this problem is to first empirically estimate the shape of phytoplankton absorption near the 440 nm absorption peak by means of the ratio  $\zeta$  ( $=a_\phi(410)/a_\phi(440)$ ) using  $r_{rs}$  bands at 440 nm and 555 nm, then to analytically calculate the ratio  $\xi$  ( $=a_{dg}(410)/a_{dg}(440)$ ) from  $S_{dg}$  using Eq. (4). The parameters  $\zeta$  and  $\xi$  are therefore representative of the spectral shape of the phytoplankton and combined detrital and dissolved absorption, respectively, in the blue portion of the spectrum. When combined with the retrieved value for  $a_{pg}(440)$ , these parameters can be used to analytically solve for  $a_{dg}(440)$ :

$$a_{dg}(440) = \frac{a_{pg}(410) - \zeta a_{pg}(440)}{\xi - \zeta} \quad (9)$$

Erroneous negative retrievals of  $a_{dg}(440)$  are eliminated (Lee et al., 2002 (none occurred within the rank 1 dataset in this study), and  $a_{dg}(\lambda)$  can be derived from  $a_{dg}(440)$ ,  $S_{dg}$ , and Eq. (4). Lastly,  $a_\phi(\lambda)$  can be solved by subtracting  $a_{dg}(\lambda)$  from  $a_{pg}(\lambda)$ . Uncertainty in algorithm retrievals attributable to the QAA (versus uncertainties in the field measurements) have been estimated here following Lee et al. (2010).

Separation of absorption into its constituents  $a_\phi$  and  $a_{dg}$  can be extremely challenging for a number of reasons. While the spectral characteristics of  $a_\phi$  and  $a_{dg}$  are distinct from each other, changes to the reflectance of surface waters deriving from the unique characteristics of each component are difficult to resolve within a limited set of spectral bands. Furthermore, as a stepwise algorithm, the QAA propagates error in the retrieval of total absorption, backscattering,  $\zeta$ , and  $\varepsilon$  in the subsequent derivation of phytoplankton, CDOM and NAP absorption constituents. Lee et al. (2010) demonstrated that error in constituent component retrievals  $a_{dg}$  and  $a_\phi$  was predominantly driven by error in total absorption retrieval, because  $\zeta$  and  $\varepsilon$  tended not to vary over a large range. Since  $a_\phi$  and  $a_{dg}$  are naturally each of smaller magnitude than total absorption, propagated errors are proportionately higher for  $a_\phi$  and  $a_{dg}$ . In fact, error propagation for  $a_\phi$  and  $a_{dg}$  is rather complex, but the authors showed with a large synthetic dataset that  $a_\phi$  is expected to have larger error than  $a_{dg}$ . For instance, uncertainty in  $a_{dg}(440)$  when  $a_{dg}(440) = 0.1 \text{ m}^{-1}$  varies from 0.02 to 0.09  $\text{m}^{-1}$ , but for  $a_\phi(440) = 0.1 \text{ m}^{-1}$ , uncertainty may vary from 0.02 to 0.70  $\text{m}^{-1}$ , meaning errors potentially seven times larger than the signal. Retrieval errors in  $a_\phi$  are likely to be compounded further in LIS waters where the phytoplankton absorption is a relatively small fraction (generally <20%) of  $a_{pg}$ , i.e. waters in which terrestrial influx of dissolved and sedimentary material dominate the absorption signature thereby decreasing the signal to noise ratio in  $a_\phi$  retrievals.

Purely analytical ocean color models do not exist and some form of empirical assumptions are required in all model formulations. Empirical relationships are dependent on the specific types of material present in a water body, such as the chemical formulation and age of CDOM, the color and minerogenic composition of NAP, and the taxonomic diversity and physiologic state of phytoplankton. No set of global empirical parameters is known to apply to all coastal regions. For a complex estuary like LIS, regional optimization is necessary to characterize the spectral dependency of the IOPs and their relationship to the reflectance ( $R_{rs}$ ) to maximize performance of an algorithm. Regional parameterization of the QAA involves optimization of the empirically derived components introduced in the previous section ( $g_0$  and  $g_1$ ,  $Y$ ,  $a(\lambda_0)$ ,  $\zeta$ , and  $S_{dg}$ ) using field measurements of  $r_{rs}$  and the relevant IOP components. Here we evaluate the robustness of the empirical parameterizations used in the foundational QAA model for each of these components and suggest improvements for the region.

## 4. Results and discussion

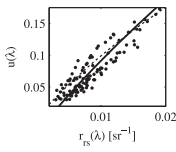
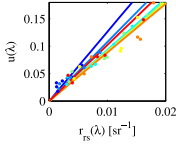
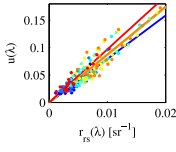
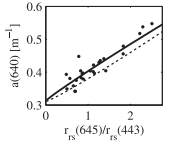
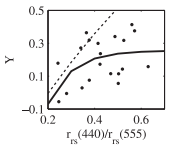
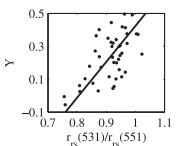
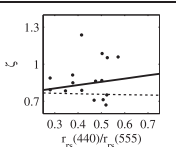
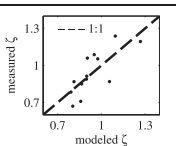
### 4.1. Bidirectionality ( $f/Q$ )

Coefficients  $g_0$  and  $g_1$  (Table 2) were calculated from field measurements of  $u(\lambda)$  and  $r_{rs}(\lambda)$  according to Eq. (1) using least-squares non-linear optimization (Press et al., 1986). Resulting coefficients ( $g_0 = 0.083$ ,  $g_1 = 0.074$ ) differed somewhat from those of Gordon et al. (1988) ( $g_0 = 0.095$ ,  $g_1 = 0.079$ ) and those suggested by Lee et al. (1999) for coastal waters ( $g_0 = 0.084$ ,  $g_1 = 0.17$ ).

Although  $r_{rs}$  modeled using  $g_0$ ,  $g_1$  regionally tuned for LIS agreed well with observations ( $r^2 = 0.86$ ,  $RMSE = 0.002$ ,  $p \ll 0.001$ , Table 2), we nevertheless found these coefficients to be somewhat sensitive to differences in optical water types across LIS. For example, depending on water type, values of  $g_0$  and  $g_1$  were not constant spectrally as assumed by most SAAs and BRDF models, and within the regional variability,  $g_1$  was not significantly different from zero (i.e., the quadratic component in Eq. (1) was negligible across the region). This is also evidenced by the linearity of the solid fit line in the first row of Table 2 as compared with the dashed fit from Lee et al. (1999). Fig. 4 and Table 3 show a closer inspection of  $g_0$  spectrally (the equivalent of  $f/Q$  assuming  $g_1 = 0$ ). Although variability is generally small, and within the ~10%–20% error inherent in measurements of backscattering (Aurin et al., 2010), we found that certain stations in LIS exhibiting extremely high red reflectances relative to blue (i.e.,  $r_{rs}(650)/r_{rs}(440) > 1.5$ ) also had more spectral variability in  $f/Q$  than others. Such high red reflectance relative to blue is indicative of waters with exceptionally high suspended sediment concentrations (i.e., high backscattering across the visible spectrum) combined with high Chl, NAP and/or CDOM (i.e., high absorption in the blue), and were all found at stations directly influenced by either the Hudson River/East River plumes in western LIS or the Connecticut River plume in eastern LIS (Fig. 5). These results are consistent with previous studies which showed that the spectral dependency of the  $f/Q$  ratio is closely tied to the biogeochemical and optical nature of the suspended particle population (Chang et al., 2007; Kostadinov et al., 2007; Morel & Gentili, 1993, 1996; Morel et al., 2002). Models and field observations of the particle phase function show considerable variability depending on optical water type, particularly in the backward direction which is most relevant for remote sensing (Berthon et al., 2007; Fournier & Forand, 1994; Petzold, 1972). In 2011, Lee et al. (2011) devised an IOP-based correction scheme for the angular effects in water-leaving radiance ( $L_u$  above the sea surface,  $L_w(\lambda, \theta^+)$ ) which considered multiple solar and viewing geometries. They found that their approach improved estimates of nadir-viewing  $L_w$  in simulated and field data, but was limited by assumptions regarding the angular shape of the particle scattering function. Furthermore, while their analysis showed considerable difference in the angular variability in  $L_w$

**Table 2**

Empirical calibration of the QAALIS. Dots are LIS data, solid lines are tuned models (this study), and dotted lines are models with original coefficients from Li et al. (2004). Starred equations indicate new models (or models different from QAA) used in this study.

Mathematical model	Data versus model	Band [nm]	r <sup>2</sup>	RMSE	n
$u(\lambda) = \frac{b_b(\lambda)}{a(\lambda) + b_b(\lambda)}$ $= \frac{-g_0 + [(g_0)^2 + 4g_1 r_{rs}(\lambda)]^{1/2}}{2g_1};$ $g_0 = 0.083, g_1 = 0.074$			0.86	0.0020	108
"Red" stations (see text) $^*r_{rs}(\lambda) = \frac{f}{Q}(\lambda) * u(\lambda)$ See Table 3 for coefficients. Colored lines (online) indicate wavebands between 412 nm and 650 nm.		412 440 488 510 532 555 650	0.86 0.98 0.96 0.95 0.92 0.89 0.91	0.0007 0.0007 0.0008 0.0011 0.0015 0.0020 0.0016	6 6 6 6 6 6 6
Remaining stations $^*r_{rs}(\lambda) = \frac{f}{Q}(\lambda) * u(\lambda)$		412 440 488 510 532 555 650	0.58 0.77 0.83 0.80 0.78 0.74 0.90	0.0012 0.0011 0.0014 0.0016 0.0018 0.0020 0.0007	21 21 21 21 21 21 21
$a(640) = 0.31 + 0.09\rho_1^{0.93};$ $\rho_1 = \frac{r_{rs}(645)}{r_{rs}(443)}$			0.85	0.022	27
$Y = 0.255(1 - 8.6 \exp(-9.5\rho_2));$ $\rho_2 = \frac{r_{rs}(440)}{r_{rs}(555)}$			0.21	0.120	20
$*Y = 2.18\rho_3 - 1.77;$ $\rho_3 = \frac{r_{rs}(531)}{r_{rs}(551)}$			0.38	0.176	50
$\zeta = \frac{a_b(410)}{a_b(440)}$ $= 16.9 - \frac{970.6}{60.1 + \rho_2};$			0.01	0.203	17
$*\zeta = \frac{a_b(410)}{a_b(440)}$ $= 1.142 - 0.151\rho_4 + 1.117Y;$ $\rho_4 = \frac{r_{rs}(551)}{r_{rs}(667)}$			0.59	0.109	13

associated with wavelength (e.g. their Fig. 7), spectral dependence was ultimately not included in their model for  $f/Q$  (i.e. the  $G$  parameters in their Eq. 14). As discussed in Section 1.1.1, most IOP-based models for correction of  $f/Q$  do not incorporate spectral variability. Furthermore, they have at best only two possible preselected particle phase functions, are parameterized for what are considered "typical" waters which often does not include optical water types found in LIS (Aurin et al., 2010), and they depend on the quasi-single scattering assumption. For example, Park and Ruddick (2005) parameterize

backscattering and scattering in their model using chlorophyll concentration, an assumption which would not hold in highly sediment-laden waters such as river outflows. Backscattering-to-scattering ratios for estimating the volume scattering function are limited to 0.010 in Lee et al. (2011) whereas those at the stations shown in Fig. 5 extend from 0.010 to 0.017. On the other hand, the CCNY model (Hlaing et al., 2012) tracks spectral variability in the BRDF, which we have shown in Fig. 4 and Table 3 to be a possible factor, at least at highly turbid river outflows. We therefore tested the



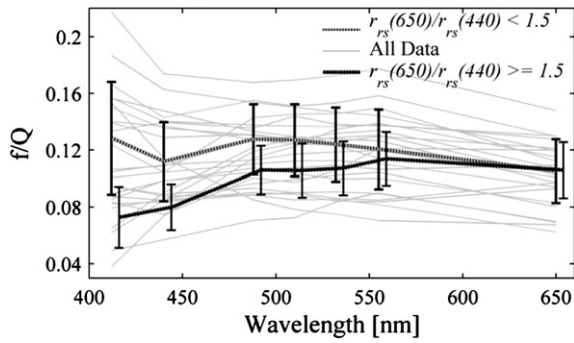


Fig. 4.  $f/Q$ , the factor relating reflectances to IOPs in LIS was found to be more spectrally dependent at stations in LIS with higher red-to-blue reflectance ratios indicative of high suspended sediment concentrations (see also Table 3, Fig. 5).

CCNY correction by running our fully tuned algorithm substituting only their BRDF model in place of our empirically derived  $f/Q$ , and report the results in Section 4.4.

An important consideration for the highly turbid stations identified in Figs. 4 and 5 and Table 3 is that the quasi-single scattering assumption may not be valid. The average single scattering albedo at these stations is  $0.82 \pm 0.02$  between 412 and 715 nm, and it has been shown that significant error can arise in estimations of reflection based on radiative transfer simplifications such as Eq. (1) when the single scattering albedo (the proportion of attenuation attributable to scattering) increases beyond  $\sim 0.6$  (Appendix A in (Gordon et al., 1975)). It is therefore quite possible that the evidence of variability in  $f/Q$  is the result of multiple scattering effects.

Using the ratio  $r_{rs}(650)/r_{rs}(440)$  to discriminate these highly sediment rich and turbid (“red”) waters yielded the spectrally dependent values for  $f/Q$  (i.e.,  $g_0$ ) shown in Table 3 and Fig. 4. Spectral variability in  $f/Q$  for these turbid stations is not dramatically different from the remaining stations at most wavebands (Fig. 4), nevertheless applying this dynamic switching approach to the algorithm increased estimates of  $b_b(\lambda)$  by an average of 17.5% and decreased  $a_{pg}(\lambda)$  by 10.8%, thereby considerably improving overall results, as described in greater detail below.

Without accurate measurements of the VSF, the exact viewing geometry (i.e. instrument nadir and azimuth angles), and sky and sea surface conditions, precise numerical modeling of the  $f/Q$  at each station would be subject to numerous assumptions (e.g. regarding the relationship between the backscattering ratio and the phase function (Fournier & Forand, 1994; Mobley, 1995), as well as realistic boundaries on the viewing geometry, solar irradiance and sea surface conditions), and was not attempted here. Nevertheless, since stations were controlled for good optical closure using numerical modeling of the light field in Hydrolight (Aurin et al., 2010; Mobley, 1995) with field IOPs and conditions, we expect that numerical model estimation of  $f/Q$  would agree well with our observations. Our results suggest that the small variability in  $f/Q$  shown in Fig. 4, because it is only evident at certain turbid stations near river outflows, derives from differences in the IOPs (i.e. the phase function or multiple scattering effects) rather than differences in

Table 3  
Spectral  $f/Q$  in LIS for highly turbid “red” waters ( $\rho > 1.5$ ), remaining waters ( $\rho < 1.5$ ); the optimized values for  $g_0$  in the QAALIS algorithm.

	Wavelength [nm]						
	412	440	488	510	532	555	650
$\rho < 1.5$	0.12599	0.11507	0.11432	0.11484	0.11443	0.11433	0.10305
$\rho > 1.5$	0.07913	0.09275	0.10684	0.10912	0.11148	0.11268	0.09772

\* $\rho = R_{rs}(650)/R_{rs}(440)$ .

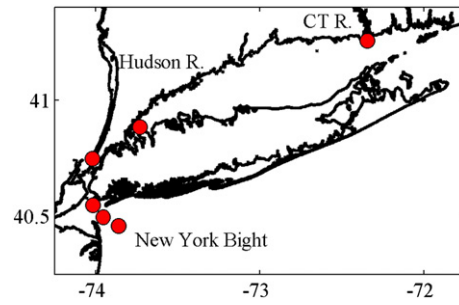


Fig. 5. Locations of stations with extremely high red reflectances as well as a spectrally varying  $f/Q$ .

solar or viewing geometry. Accounting for this variability significantly improves model retrievals at these stations (see sensitivity analysis in Section 4.4).

#### 4.2. Red reference channel

The QAA640 requires an initial empirical estimate of  $a(640)$  from measurements of  $r_{rs}$  in the red portion of the spectrum, ( $r^2 = 0.85$ ,  $RMSE = 0.022$ , Table 2). The reference waveband need not be exactly 640 nm, but should be located somewhere on the spectrum between approximately 600 and 650 nm. To help illustrate why a red reflectance channel in this range is crucial for remote sensing of turbid water, we consider the individual spectral absorption contributions for a typical station in LIS (Fig. 6). In the blue-green portion of the spectrum, absorption is dominated by particulate and dissolved substances in the water ( $a_{pg}$ ), while at wavelengths between  $\sim 600$  nm and  $\sim 650$  nm, water absorption is strongest. Further in the red, the strong *in vivo* chlorophyll-a absorption peak centered near 676 nm in  $a_{cp}$  and  $a_{pg}$  can reach or even exceed absorption by seawater in the most productive waters and can often be observed as a trough in the spectral remote sensing reflectance (e.g. Fig. 8 in Aurin et al., 2010). In turbid coastal waters or river plumes, particulate and dissolved absorption at 555 nm is significantly higher than  $a_w$ . Even in areas of lower productivity within LIS, high concentrations of NAP (predominantly sediment) and CDOM typical of the region cause absorption in the green to be dominated by the particulate and dissolved components. Near 640 nm, however, water absorption is stronger than  $a_{pg}$ , even in the turbid LIS estuary (Fig. 6). Errors in the initial estimates of  $a_{pg}$  at this waveband should only represent a fraction of the total absorption (i.e. as compared with estimates at 555 nm or 440 nm where  $a_{pg} \gg a_w$ ), and the variability in total

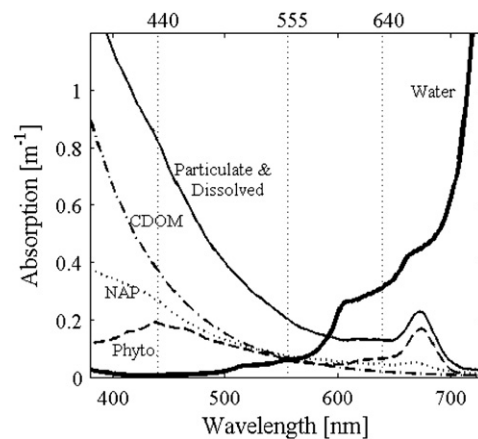


Fig. 6. Constituent absorption spectra for a typical station in LIS illustrating a predominance in particulate and dissolved absorption at 440 nm and 555 nm compared with 640 nm.

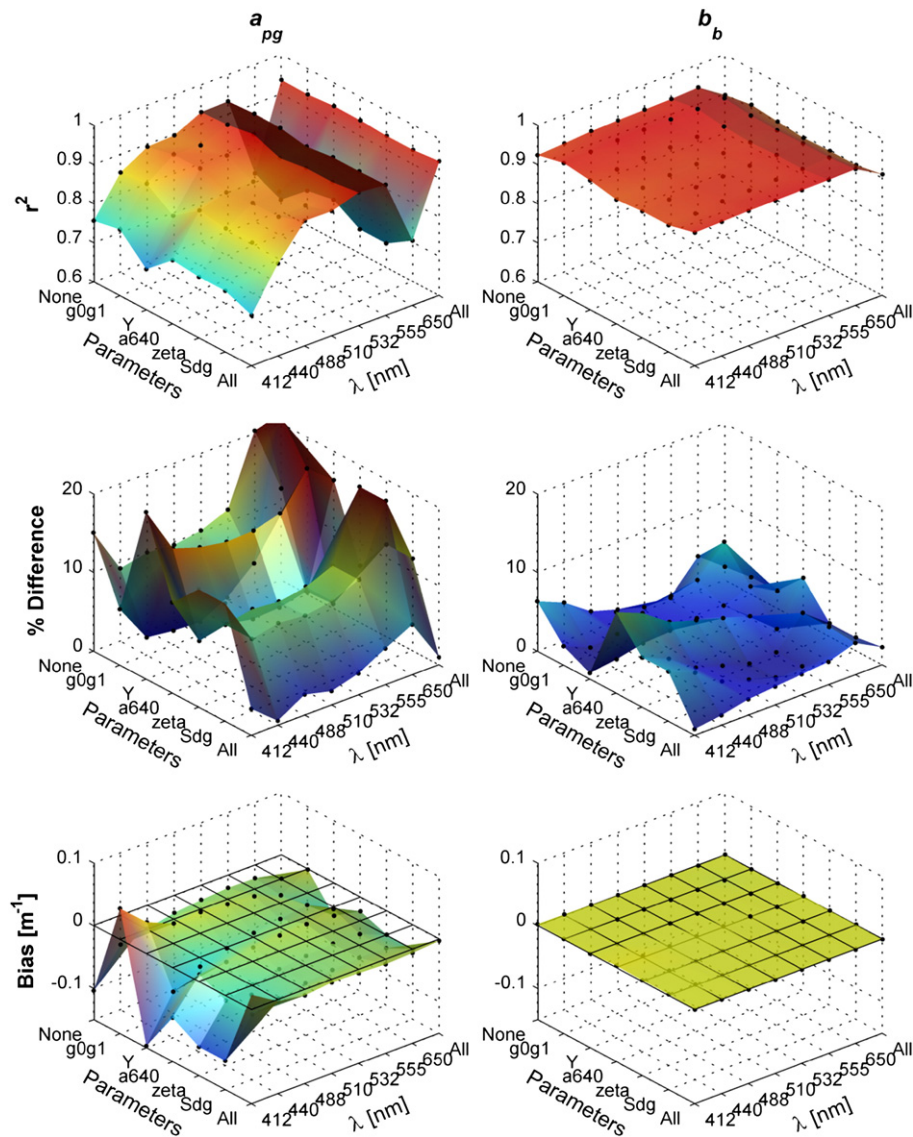


Fig. 7. Sensitivity of model performance (z-axes) as a function of empirical tuning parameters (x-axes) and wavelength of retrieval (y-axes). Metrics for all tuning parameters combined is shown at the end of the x-axes, and for all wavelengths combined at the end of the y-axes.

absorption due to the addition of  $a_{pg}$  has been estimated at 2- and 20-fold, respectively Lee et al. (2002)), thereby reducing error in the inversion of the backscattering coefficient at the reference wavelength. In extremely turbid waters, however, CDOM and NAP may dominate absorption at 640 nm and new model formulations may consider using a reference wavelength in the near infrared (channels commonly used for image atmospheric correction). A recent study in the highly turbid waters of Taihu Lake in China found that shifting the reference wavelength from 640 nm into the near infrared was instrumental in improving retrievals of the absorption coefficient (Le et al., 2009).

#### 4.3. Spectral shape parameters $Y$ , $\zeta$ , and $\xi$

For practical reasons,  $Y$ , the spectral slope of *in situ* measurements of  $b_{bp}$ , was estimated in LIS from the spectral slope of  $b_p$  as described in Aurin et al. (2010). This approach assumed a spectrally independent backscattering ratio and was supported by Mie theory (Ulloa et al., 1994) and field data (Whitmire et al., 2007), although studies have challenged this assumption for natural waters (McKee & Cunningham, 2005; Snyder et al., 2008), and more extensive

multi-spectral measurements of  $b_{bp}$  in LIS are clearly warranted.  $Y$  has been shown to be related to the particle size distribution, whereby polydispersions of larger particles such as those found in coastal and estuarine waters tend to lead to a weaker spectral dependence in  $b_{bp}$  (Babin et al., 2003; Morel & Ahn, 1990), although empirical corroboration remains limited. For retrieving  $Y$  from  $r_{rs}$  (i.e., step 4 in Table 2 of Lee et al. (2002)), we found that a simple linear fit to  $r_{rs}(531)/r_{rs}(555)$  (Table 2, this study) proved more robust in LIS ( $r^2=0.38$ , RMSE=0.176) than the original exponential model ( $r^2=0.21$ , RMSE=0.120,  $p=0.017$ ,  $n=20$ ) tuned to LIS. Retrieving  $Y$  from  $r_{rs}$  is especially challenging in near shore waters where spectral dependence is expected to be fairly weak, and this is reflected in the weak correlations between the two parameters. However, the algorithm proved overall to be relatively insensitive to empirical estimates of  $Y$  (see Section 4.4).

Within the somewhat limited  $a_\phi$  data availability in LIS,  $\zeta$ , the parameter describing the spectral shape of  $a_\phi$  in the blue (see Section 3.1), did not correlate with band ratios suggested in Lee et al. (2002). The best relationship to retrieve  $\zeta$  involved multiple regression with both an  $r_{rs}$  band ratio ( $r_{rs}(551)/r_{rs}(667)$ ) and our previously retrieved value for  $Y$  (Table 2,  $r^2=0.59$ , RMSE=0.109,

$p < 0.01$ ,  $n = 13$ ). The difficulty in finding a more robust relationship suggests that deriving the shape of phytoplankton absorption (i.e.  $\xi = a_{\phi}(410)/a_{\phi}(440)$ ) from ocean color is very challenging in waters like those in LIS, which tend to have stronger absorption in the blue from CDOM and NAP than from phytoplankton. In fact, we found that among rank 1 stations,  $a_{\phi}(440)/a_{pg}(440)$  varied between just 2% and 24%. The choice to incorporate  $Y$  in this component of the model follows from the consideration that together with the spectral characteristics of  $a_{dg}$  and  $a_{\phi}$ ,  $Y$  also has an effect on the slope of  $r_{rs}$  between 551 nm and 667 nm. We also found that a small empirical adjustment to  $a_{dg}(440)$  prior to spectral extrapolation ( $a_{dg}(440) = 0.33(a_{dg}(440) + 0.4)$ ) moderately improved waveband-specific  $a_{dg}$  retrievals (see below). To solve for  $\xi$ , which describes the spectral shape of  $a_{dg}$  in the blue ( $\xi = \exp[S_{dg}(440-410)]$ ), we used the regional average for  $S_{dg} = 0.0134 \pm 0.0013$ , which was shown not to deviate significantly across the region or between seasons in LIS (Aurin et al., 2010).

#### 4.4. Sensitivity analysis of model parameters

A sensitivity analysis was performed to evaluate the importance of each empirical tuning parameter by comparing retrievals of the principal parameters ( $a_{pg}$  and  $b_b$ ) with field data. This approach identified the empirical components of the algorithm with the most beneficial impact on model performance. Each element was tuned independently, and the improvement to retrievals was evaluated as a function of each parametric component, as well as the wavelength retrieved (Fig. 7). All tuned empirical elements were then combined to assess overall model performance. A caveat to this analysis is that ideally algorithm validation would employ an independent dataset from that used in the tuning models to test algorithm performance and sensitivity, but owing to the relatively small number of stations remaining after quality selection (particularly for  $a_{\phi}$  and  $a_d$  data), separation into “tuning” and “validation” sets was impractical.

As described in Lee et al. (2002) the empirical elements of the QAA have secondary order of importance compared with the analytical portions of the algorithm (i.e., inversion of Eq. 1). Sensitivity of the algorithm to tuning parameters was evaluated for wavebands centered at 412, 440, 488, 510, 532, 555 and 650 nm. At longer wavelengths, good retrievals are generally precluded owing to the dominance of seawater in the total absorption spectrum which obscures the signature of the suspended and dissolved constituents in the sea-surface reflectance. Results for all wavelengths combined are included as the last parameter of the ordinate axes in Fig. 7.

Tuning of the empirical parameters generally produced only small improvement in overall correlations between observed and modeled  $a_{pg}$  and  $b_b$ . Tuning the  $g_0 g_1$  parameters (i.e. using  $f/Q$  and a water-type switching algorithm as described above) shows the most dramatic improvement for retrieving  $a_{pg}$  and  $b_b$ , e.g. lowering PD from 9.2% to 2.2% for retrievals of  $a_{pg}(440)$ , and from 4.9% to 1.0% for  $b_b(440)$ , while bias is reduced from  $0.05 \text{ m}^{-1}$  to  $0.01 \text{ m}^{-1}$  and from  $0.0014 \text{ m}^{-1}$  to  $0.0003 \text{ m}^{-1}$  for  $a_{pg}(440)$  and  $b_b(440)$ , respectively. Tuning  $a(640)$  is also important for  $a_{pg}$ , e.g. reducing PD from 9.2% to 5.4% and bias from  $0.05$  to  $0.03 \text{ m}^{-1}$  for  $a_{pg}(440)$ . For  $a_{pg}$ , tuning both  $f/Q$  and  $a(640)$  has a strong synergistic effect, and reduced PD from 9.2% to 0.6% and bias from  $0.05$  to  $0.003 \text{ m}^{-1}$  for  $a_{pg}(440)$ . Tuning  $Y$  is important for  $b_b$ , e.g. reducing PD from 4.9% to 1.2% and bias from  $0.0014$  to  $0.0004 \text{ m}^{-1}$  for  $b_b(440)$ .

The  $r^2$  for  $a_{pg}$  retrievals shows a marked sensitivity to wavelength of the retrievals, with peak  $r^2$  occurring at 555 nm and declining gradually toward the blue, and steeply at 650 nm. Deterioration of retrieval quality in the red is almost paradoxically a result of the dominance of water absorption at longer wavelengths obscuring the absorption signature of suspended and dissolved constituents in the reflectance. Deterioration in the blue is likely due to errors in spectral extrapolation of retrievals from the reference wavelength (640 nm) by means of the backscattering shape parameter,  $Y$ , with no *a priori* knowledge of the spectral shape of  $a_{pg}$ .

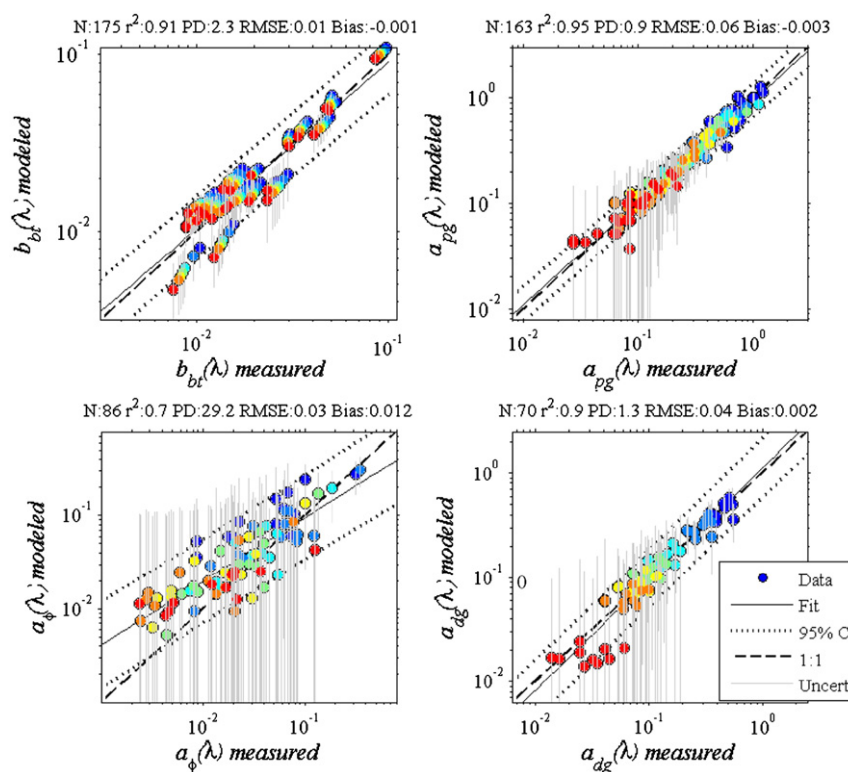


**Fig. 8.** Performance of the model for retrieval of  $b_b(\lambda)$ ,  $a_{pg}(\lambda)$ ,  $a_{\phi}(\lambda)$ , and  $a_d(\lambda)$ . Colors of dots (available online) represent appropriate wavelengths 412 nm–650 nm. Uncertainties (gray lines) are calculated following Lee et al. (2010), and typically overlapped the 1:1 line (dashed line). Retrievals fell within or overlapped the 95% confidence intervals (dotted lines) shown above and below the model fit (solid line).



**Table 4**  
Comparative algorithm retrievals prior to (QAA640) and after optimization for LIS (QAALIS) as in Fig. 9. Improvements of 50% or more shown in bold.

	QAA640				QAALIS			
	$a_{pg}$	$a_{dg}$	$a_{\phi}$	$b_b$	$a_{pg}$	$a_{dg}$	$a_{\phi}$	$b_b$
$r^2$	0.94	0.92	0.29	0.90	0.95	0.90	<b>0.70</b>	0.91
PD	1.9	4.9	249.0	2.6	<b>0.9</b>	<b>1.3</b>	<b>29.2</b>	2.3
RMSE	0.254	0.069	0.148	0.009	<b>0.063</b>	<b>0.039</b>	<b>0.033</b>	0.007
Bias	-0.008	0.011	0.098	0.001	<b>-0.003</b>	<b>0.002</b>	<b>0.012</b>	-0.001
Slope	1.07	1.25	0.60	0.90	<b>0.99</b>	<b>1.13</b>	<b>0.80</b>	<b>1.00</b>
Intercept	-0.003	0.167	-0.018	-0.121	<b>-0.011</b>	0.107	<b>-0.145</b>	<b>-0.023</b>

Performance metrics and retrieval uncertainty of the regionally optimized model for  $b_b$ ,  $a_{pg}$ ,  $a_{\phi}$ , and  $a_{dg}$  are shown in Fig. 8 for all wavelengths combined. Retrievals of  $b_b$ ,  $a_{pg}$ , and  $a_{dg}$  correlated very well with field measurements ( $r^2 = 0.91, 0.95,$  and  $0.90$ , respectively) with low bias and RMSE, and low PD. Retrieval uncertainty for all parameters fell within or overlapped the 95% prediction confidence interval (dotted lines Fig. 8), and generally overlapped the 1:1 (dashed) line, although some bias in the  $b_b$  retrievals at low magnitudes was apparent. In general, increased uncertainty and error at very low magnitude retrievals of  $b_b$  and  $a_{pg}$  (i.e., less than  $\sim 0.010 \text{ m}^{-1} b_b$  or  $\sim 0.10 \text{ m}^{-1} a_{pg}$ ) is apparent; likely a result of the fact that the QAALIS is optimized for the highly scattering ( $b_b(440) = 0.018 \pm 0.029 \text{ m}^{-1}$  for the optimization data set) and absorbing ( $a_{pg}(440) = 0.575 \pm 0.379 \text{ m}^{-1}$ ) waters of LIS. The same phenomenon is also pronounced in retrievals of  $a_{dg}$  and  $a_{\phi}$ , which are of considerably lower magnitude than  $a_{pg}$  relative to error and uncertainty.

As expected (see Section 3.2 and Lee et al. (2010)), second tier retrievals  $a_{dg}$  and  $a_{\phi}$  are more susceptible to error than  $a_{pg}$  and  $b_b$ . Nevertheless,  $a_{dg}$  and  $a_{\phi}$  retrievals with the QAALIS show significant improvement over the non-optimized QAA640 algorithm (Table 4 and Fig. 9). Improvements over the QAA555 and other SAAs evaluated here are considerably higher (e.g. see Fig. 3).

The fully tuned inversion algorithm was also evaluated after changing only the  $f/Q$  correction factor to the CCNY third degree polynomial model interpolated to our wavebands. In general, retrievals using the CCNY correction performed well with coefficients of determination comparable to the untuned QAA640 (e.g.  $r^2 = 0.90, 0.94, 0.90$  for  $b_b, a_{pg},$  and  $a_{dg}$ , respectively) and only a small increase in error for  $b_b, a_{pg}, a_{dg}$  (e.g. PD = 8.4%, 9.1%, 17.8%, and bias =  $0.002 \text{ m}^{-1}, -0.030 \text{ m}^{-1}, -0.030 \text{ m}^{-1}$ , respectively) compared with those of the untuned QAA640 (Table 4). For  $a_{\phi}$ , PD and bias actually decreased to 27.2% and  $0.011 \text{ m}^{-1}$ , respectively – slightly lower even than the QAALIS – but the  $r^2$  decreased from 0.70 to 0.61.

Aggregate statistics can be misleading for parameters that have strong wavelength dependence (e.g.,  $a_{dg}$ , Fig. 8), so the model is also evaluated at each wavelength individually. Retrieved  $b_b, a_{pg}, a_{dg},$  and  $a_{\phi}$  are compared to measured parameters at individual wavebands (Figs. 10–13). Retrievals of backscattering are excellent across all wavebands (Fig. 10). Bulk absorption ( $a_{pg}$ ) retrievals are best between 488 nm and 555 nm, and exhibited a moderate negative bias at 650 nm, where it also has the largest uncertainties (Fig. 11). Uncertainties and error in  $a_{\phi}$  and  $a_{dg}$  tend to be much higher, as expected for the reasons outlined above. While the algorithm appears to capture the overall magnitude of  $a_{dg}$  quite well across all wavebands (Fig. 8), it is

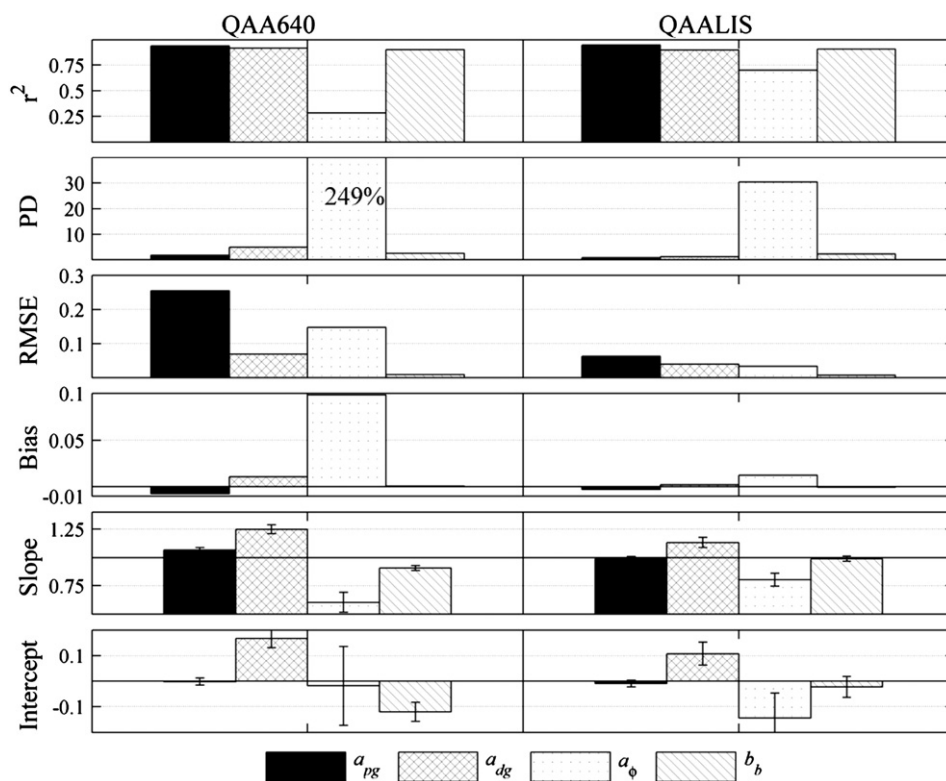


**Fig. 9.** Improvements in algorithm performance for retrieving  $a_{pg}$ ,  $a_{dg}$ ,  $a_{\phi}$ , and  $b_b$  across all wavebands deriving from regional optimization.



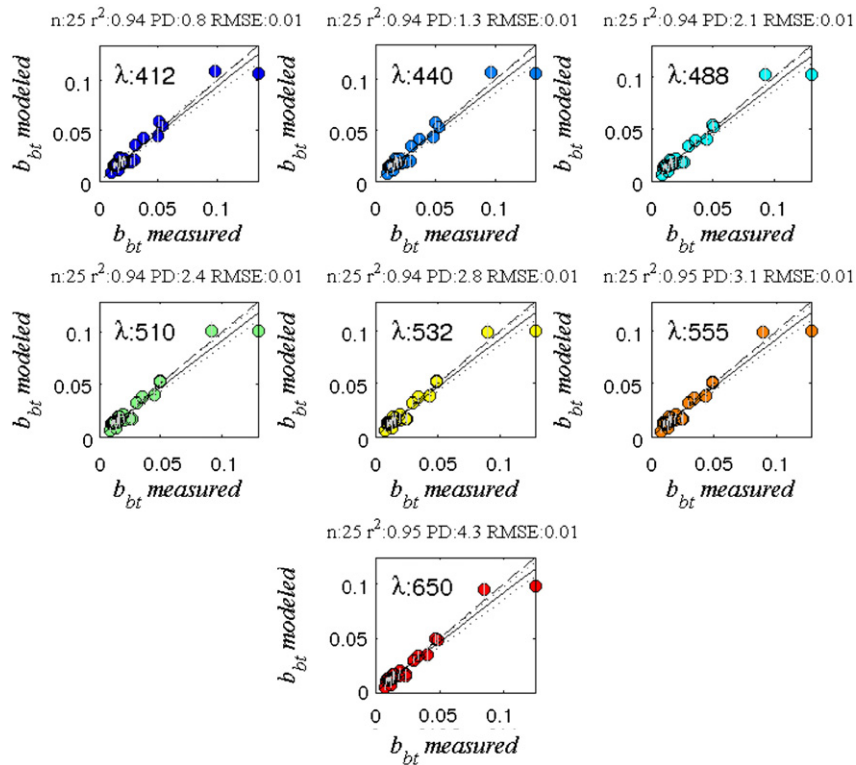


Fig. 10. Waveband specific QAALIS retrievals of total backscattering ( $b_{bt}$ ) compared with field measurements, and statistical performance metrics for each band.

less accurate on a wavelength-specific basis (Fig. 12), though retrievals fall within the large uncertainties. Correlations between modeled and measured  $a_{\varphi}(\lambda)$  are variable ( $0.66 < r^2 < 0.90$ ) and likely inflated by the singleton high value, while PD and RMSE are generally high (Fig. 13).

Performance of the algorithm for retrieving phytoplankton absorption  $a_{\varphi}$  is less than optimal (Figs. 8 and 13), despite an empirical correction to retrievals ( $a_{\varphi}(\lambda) = 0.33a_{\varphi}(\lambda)$ ) which brings retrievals closer to the 1:1 line. Each phytoplankton taxonomic group has distinctive absorption characteristics (e.g. Johnsen et al., 1994; Roesler

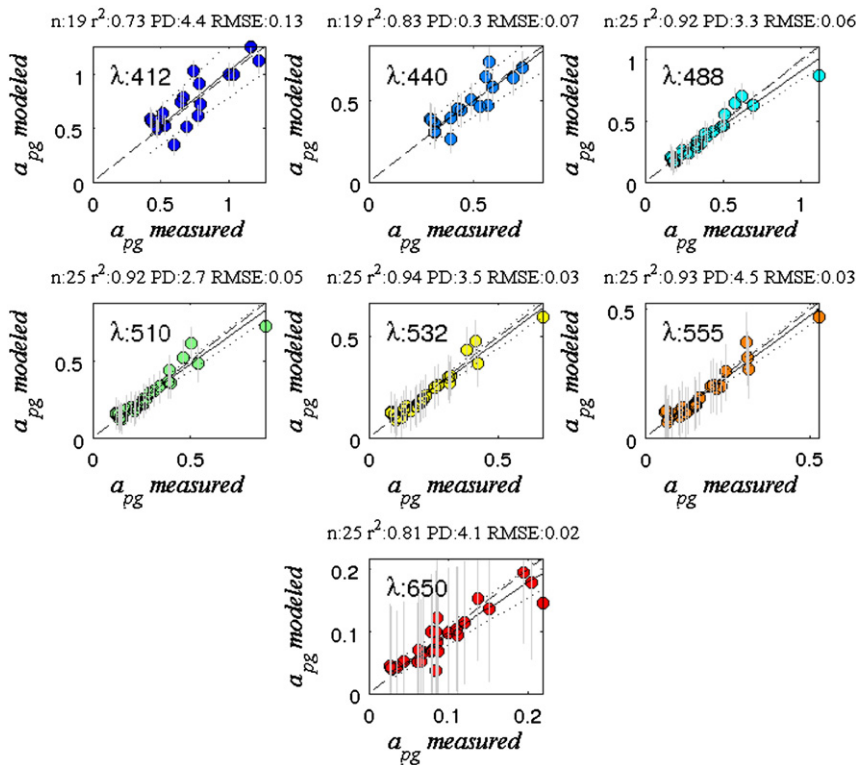


Fig. 11. Waveband specific QAALIS retrievals of total absorption ( $a_{pg}$ ) compared with field measurements, and statistical performance metrics for each band.

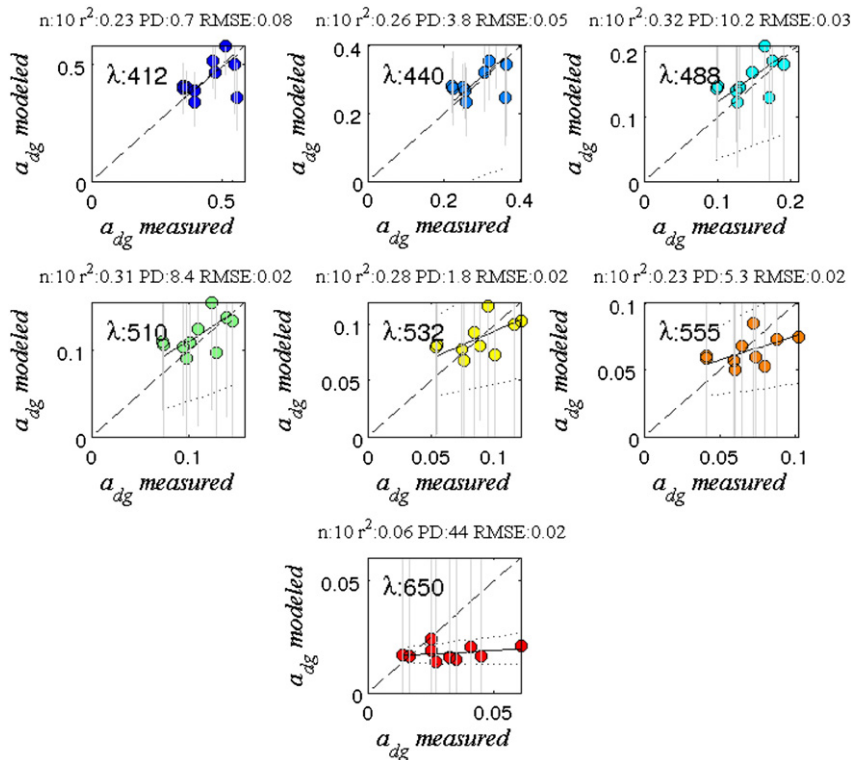


Fig. 12. Waveband specific QAALIS retrievals of combined dissolved and non-algal absorption ( $a_{dg}$ ) compared with field measurements, and statistical performance metrics for each band.

et al., 1989). In addition to the error propagation discussed above, the highly diverse composition of phytoplankton assemblages found in LIS may contribute to the sub-optimal performance in  $a_{\phi}(\lambda)$ . Fig. 14 shows seasonal phytoplankton taxonomic distribution across the study area based on analysis of HPLC pigment data using pigment

ratios specific to LIS (see Section 2.1). Unsurprisingly, diatoms are prevalent in these high nutrient waters during all seasons and nearly all sub-regions. Cryptophyceae and prymnesiophyceae are common during winter in eastern and western LIS, respectively. Crysophyceae are most prevalent in spring, and can be found mainly in central and

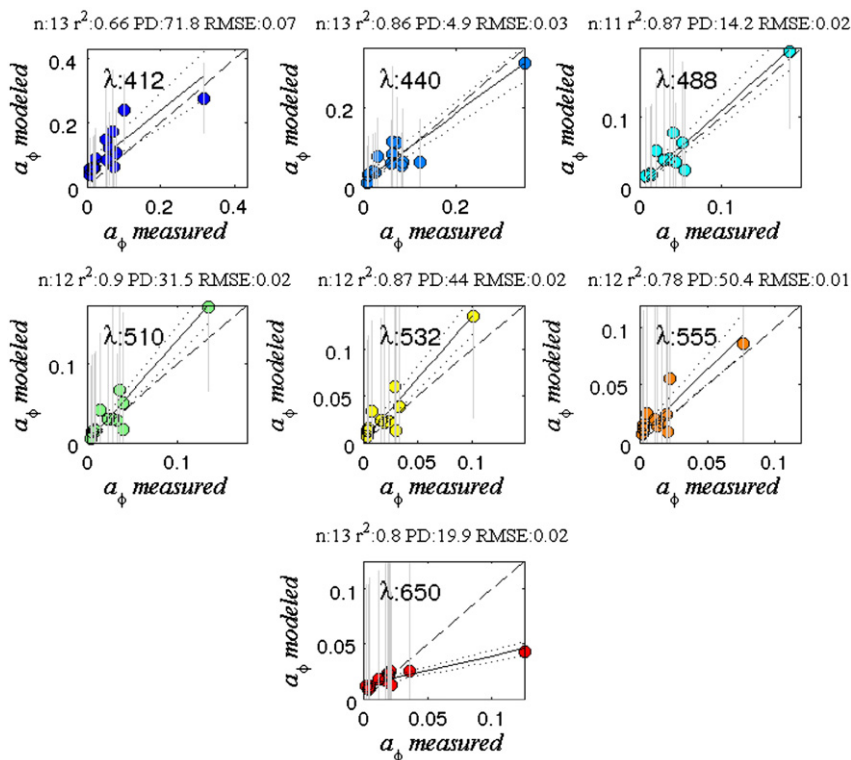


Fig. 13. Waveband specific QAALIS retrievals of phytoplankton absorption ( $a_{\phi}$ ) compared with field measurements, and statistical performance metrics for each band.

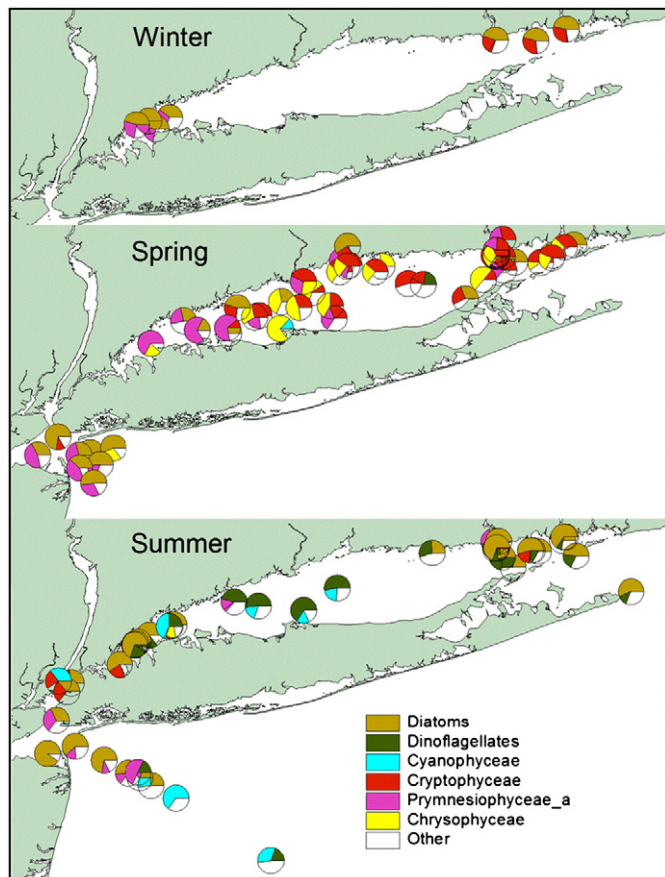


Fig. 14. Seasonal phytoplankton taxonomic groups based on HPLC pigment analysis using pigment ratios specific to LIS (see text). For clarity, only the two most prevalent taxonomic groups at each station are shown explicitly.

eastern LIS. In summer, dinoflagellates are widespread throughout LIS, but they are uncommon in winter and spring. The diversity in phytoplankton taxa found in this study agrees with earlier studies conducted in LIS by the Connecticut Department of Environmental Protection (CTDEP, 2005). Unfortunately, within the limited number of rank 1 stations with HPLC measurements ( $n = 18$ ), no discernible patterns were found between the quality of  $a_{\varphi}(\lambda)$  retrievals and phytoplankton taxonomic groups, sub-region, season, or particle size distribution. Nevertheless, the diversity of phytoplankton shown in Fig. 14 partially explains the high variability found in chlorophyll-specific phytoplankton absorption (see next section) in LIS (Aurin et al., 2010), and suggests that higher spectral resolution in  $R_{rs}$  may be necessary to distinguish the  $a_{\varphi}$  signature from  $a_{dg}$ .

In fact, while the QAA performs very well in retrieving  $a_{pg}$ ,  $a_{dg}$ ,  $b_b$ , and TSM in LIS, it may not be the best candidate for accurately retrieving  $a_{\varphi}$ , because – as discussed above –  $a_{\varphi}$  is effectively the quaternary product of this stepwise algorithm, aggregating error from estimates of  $a(\lambda_0)$ ,  $b_b$ ,  $Y$ ,  $a_{pg}$ ,  $\zeta$ ,  $\varepsilon$ , and  $a_{dg}$ . Phytoplankton diversity may also play a role, but more data are needed to explore the relationships between taxa and retrieval performance.

#### 4.5. Bio-optical models for Chl and TSM

Phytoplankton absorption is roughly proportional to the concentration of phytoplankton and the chlorophyll-specific phytoplankton absorption (i.e.,  $a_{\varphi}^*(\lambda) = a_{\varphi}(\lambda)/Chl$ ). Therefore, retrievals of light absorption by phytoplankton  $a_{\varphi}$  are often used in conjunction with an *a priori* estimate of chlorophyll-specific absorption  $a_{\varphi}^*$  to derive Chl. However, the chlorophyll-specific absorption varies considerably with phytoplankton size and pigment composition. For example,

pigment packaging effects associated with larger cell sizes common to estuarine waters decrease  $a_{\varphi}^*$  with increasing Chl (Ciotti et al., 2002), while changes in pigment composition associated with changes in speciation, light availability, and nutrient stress can also lead to variability in  $a_{\varphi}^*$ , particularly in the blue (Soret) phytoplankton absorption band (e.g., Bricaud et al., 1995; Hoepffner & Sathyendranath, 1993). We found no predictable relationship between  $a_{\varphi}^*$  and Chl, as commonly found in open ocean waters (Bricaud et al., 1995), nor between  $a_{\varphi}^*$  and taxonomic composition or particle size distribution. To retrieve Chl, it was therefore necessary to use a regional average value for  $a_{\varphi}^*(0.016 \pm 0.010 \text{ m}^2 \text{ mg}^{-1}$  at 440 nm) which is within the range of published values for coastal, productive waters with generally larger cell sizes (Brewin et al., 2011; Mitchell & Kiefer, 1988). The QAA as published does not retrieve Chl, but Chl retrieved by the QAALIS using this approach shows a significant improvement over the standard OC3M algorithm designed for MODIS ( $r^2$  increased from 0.33 to 0.59, PD reduced from 21.6% to 12.3%, and bias reduced from 1.18 to  $-0.8$ , Fig. 15a). New ocean color sensors with additional spectral channels across the visible spectrum may aid in discerning subtle spectral shifts in absorption spectra and the resulting impact on reflected color (Dierssen et al., 2006). High resolution spectral information between 430 and 500 nm, for example, has been used elsewhere to differentiate distinct absorption features of diatoms and cyanobacteria (Chang et al., 2004; Ryan et al., 2005). Determining whether these approaches can be successful in waters like LIS where between 60% and 97% (median 89%) of particulate and dissolved absorption is attributable to  $a_{dg}$  rather than  $a_{\varphi}$  will require more data and further investigation.

Total suspended material (TSM) has been historically retrieved from remote sensing imagery using empirical relationships between the reflectance and TSM (e.g., Kirk, 1994) and references therein). An increase in TSM in the water column proportionally increases the backscattering coefficient and coincident reflectance, primarily in wavebands with low constituent absorption. Empirical retrieval of TSM from reflectance data has the advantage of being simple and

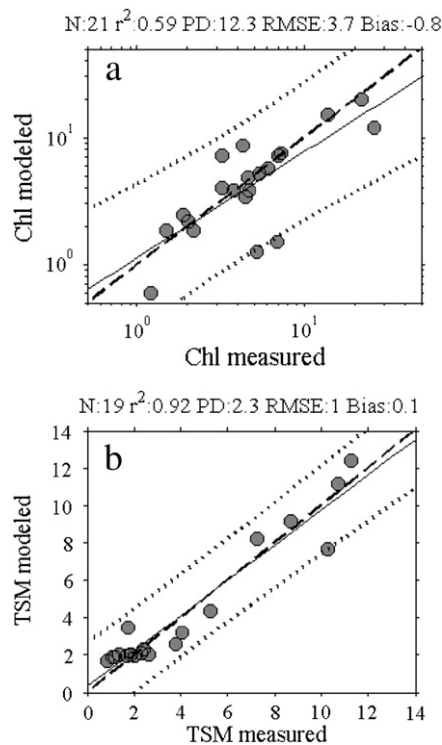


Fig. 15. QAALIS retrievals of a) Chlorophyll and b) Total Suspended Matter from *in situ* measurements of spectral reflectance in Long Island Sound.



easy to implement (Bowers & Binding, 2006; Dekker et al., 2001, 2002; Kirk, 1994; Müller & McKee, 2004), but the derived regression coefficients vary widely by region depending on the absorption, particle size distribution, and refractive index properties of the suspended material. Here, TSM modeled using the coefficients from a linear least-squares fit of TSM to *in situ* measurements of either  $b_b(660)$  or  $R_{rs}(645)$  (slope = 95.0 or 811.1 respectively; intercept = 5.8 or 0.7 respectively) had lower error and higher correlation using  $b_b(660)$  than  $R_{rs}(645)$  (RMSE = 0.0006 versus 0.0009;  $r^2 = 0.91$  versus 0.81, respectively). Modeling TSM from the QAALIS-retrieved values of  $b_b(660)$  using these coefficients produced very good retrievals of TSM from ~1 to 10 mg L<sup>-1</sup> ( $r^2 = 0.92$ , Fig. 15b), and is less subject to error propagation in the QAA than Chl because it is not influenced by error in retrievals of absorption components (with the exception of  $a(\lambda_0)$ ).

## 5. Summary

Various semi-analytical algorithms for ocean color remote sensing were tested for their ability to retrieve IOPs, Chl, and TSM in the optically complex waters of Long Island Sound, an urban estuary on the east coast of the United States. Comparison to field measurements revealed that the best semi-analytical model for these highly scattering, turbid waters was the quasi-analytical algorithm (Lee & Carder, 2002, 2004; Lee et al., 2006, 2010). The QAA lends itself easily to optimization of its stepwise, component models which can be tuned independently (i.e. unlike training neural networks, spectral matching as in LMI algorithms, or simulated annealing optimization as in GSM01), and does not require *a priori* assumptions regarding the spectral shapes of retrieved IOPs. Unfortunately, the stepwise nature has the disadvantage that error propagates from its first total absorption retrieval at  $\lambda_0$ , to multispectral backscattering, multispectral absorption, and then to absorption components for phytoplankton, non-algal and dissolved constituents, and ultimately to Chl. TSM is less susceptible to error propagation because it is derived from  $b_b$ , which is essentially the primary retrieval parameter of the QAA. It has been shown elsewhere that this error propagation can lead to large errors in  $a_\varphi$  compared with the other retrieval constituents including  $a_{dg}(\lambda)$  (Lee et al., 2010), a finding which is confirmed here.

Retrievals of bio-optical properties with a spectral reference band at 640 nm showed significant improvement over the standard 555 nm band because total light absorption near 640 nm is primarily greatest for seawater itself rather than for other constituents in the water column. This remains a good reason to include such a channel, located between ~600 and 650 nm, in future satellite missions. Optimizing the model in a spectral region with known absorption minimizes the inevitable propagation of error arising from the initial empirical estimate of  $a(\lambda_0)$ . Thus, the model can better deconvolve the influence of absorption and backscattering on the reflected color, and it produced the best retrievals of  $a_{pg}(\lambda)$  and  $b_b(\lambda)$  compared to the other semi-analytical models tested here.

In optimizing the model for LIS, the most significant change in the formulation of the QAA is the use of a spectrally varying, water-type dependent  $f/Q$  factor. This factor, which accounts for the bidirectional nature of the upwelling radiance field, is a function of solar and viewing geometry, atmospheric conditions, and the IOPs themselves — particularly the volume scattering function. Using radiative transfer modeling, Morel et al. (2002) showed that dependence of  $f/Q$  on the viewing geometry and atmospheric conditions is weak within the remote sensing domain (see Section 4.1), but spectral variability is significant for very low Chl (0.03 mg m<sup>-3</sup>) and for high Chl (10 mg m<sup>-3</sup>). Similar results were found in field studies in the Santa Barbara Channel in Southern California (Chang et al., 2007; Kostadinov et al., 2007). In this study, spectral variability in  $f/Q$  was prominent in only a handful of turbid, sediment-laden stations near the outflows of the Connecticut and Hudson Rivers (Figs. 4 and 5) — stations that can be identified remotely by

their high reflectances in the red — indicating that the variability derives from water column properties rather than viewing geometry or atmospheric conditions. The recently introduced CCNY BRDF model also contains spectral variability (although not the ability to vary with optical water type). It was therefore tested in our inversions and found to perform fairly well, but did not improve retrievals over the untuned QAA640 algorithm.

Despite optimization, retrievals of phytoplankton-related parameters, such as  $a_\varphi(\lambda)$  and Chl, were less accurate than other parameters. Lee et al. (2010) demonstrated that error in  $a_\varphi$  is expected to be higher than other retrieval parameters for several reasons, but principally because it is susceptible to error propagation from all other retrieval parameters combined. This error may be considerably reduced in waters where  $a_\varphi$  and  $a_{dg}$  are of relatively comparable magnitudes (i.e.  $0.06 < a_{dg}(440)/a_\varphi(440) < 2$ ), but in the CDOM and particle-laden waters of LIS,  $a_{dg}(440)/a_\varphi(440)$  ranges from 3.6 to 30.0 (Aurin et al., 2010). Moving away from a stepwise model for retrieving  $a_\varphi$  in waters where  $a_\varphi \ll a_{dg}$  should enhance our ability to assess phytoplankton biomass from space in the complex waters. Phytoplankton assemblages across the region derived from HPLC pigment analysis showed remarkable diversity including significant relative populations of cyanophyceae, prymnesiophyceae, chrysophyceae and cryptophyceae, in addition to the expected dominance of diatoms and dinoflagellates (Fig. 14). Given the diversity of taxonomic assemblages and variability in  $a_\varphi^*$  in LIS, accurate derivations of Chl and other phytoplankton-related parameters (e.g., primary productivity) is likely to require more spectral information than is available from multi-spectral sensors and is the subject of future research.

Optimization and refinement of ocean color remote sensing algorithms in optically complex regions such as LIS are necessary for the synoptic study of diverse environmental issues such as sediment transport, light availability for seagrasses, eutrophication, and budgets of dissolved and particulate carbon and other elemental constituents. Inherent optical properties retrieved from space are critical to furthering our understanding of light penetration in the water column and the biogeochemical processes in coastal and estuarine waters. For example, the dissolved and particulate concentration parameters retrieved here are useful for assessing riverine discharge, mixing and residence times of surface waters, as well as assessing the turbidity and light penetration in this estuary. Even in one of the most optically complex, dynamic, and diverse estuaries in the U.S., we demonstrate here that given regional optimization and the proper wavebands, ocean color can be successfully used to estimate key optical and biogeochemical properties.

## Acknowledgments

This work was funded in part by the Department of Defense National Defense Science and Engineering Graduate Fellowship, National Aeronautic and Space Administration Ocean Biology and Biogeochemistry research program (NNG04GN61G to H.M. Dierssen), and the University of Connecticut. Many thanks to the Long Island Sound Integrated Coastal Observation System (LISICOS) and the crew on the R/V Connecticut, to Scott Freeman, Brandon Russell, and Kelley Bostrom for providing optical field data, and to Emmanuel Boss and Steve Ackleson for equipment and ship time provided in support of the project.

## References

- Arnore, R., Babin, M., Barnard, A. H., Boss, E., Cannizzaro, J. P., Carder, K. L., et al. (2006). Report 5: Remote sensing of inherent optical properties: fundamentals, tests of algorithms, and applications. Dartmouth, CA: International Ocean-Colour Coordinating Group.
- Aurin, D. A., Dierssen, H. M., Twardowski, M., & Roesler, C. (2010). Optical complexity in Long Island Sound and implications for coastal ocean color remote sensing. *Journal of Geophysical Research*, 115.



- Babin, M., Morel, A., Fournier-Sicre, V., Fell, F., & Stramski, D. (2003). Light scattering properties of marine particles in coastal and open ocean waters as related to the particle mass concentration. *Limnology and Oceanography*, 48, 843–859.
- Behrenfeld, M. J., Westberry, T. K., Boss, E. S., O'Malley, R. T., Siegel, D. A., Wiggert, J. D., et al. (2009). Satellite-detected fluorescence reveals global physiology of ocean phytoplankton. *Biogeosciences*, 6, 779–794.
- Berthon, J.-F., Shybanov, E., Lee, M. E. G., & Zibordi, G. (2007). Measurements and modeling of the volume scattering function in the coastal northern Adriatic Sea. *Applied Optics*, 46, 5189–5203.
- Blondeau-Patissier, D., Brando, V. E., Oubelkheir, K., Dekker, A. G., & Daniel, P. (2009). Bio-optical variability of the absorption and scattering properties of the Queensland inshore and reef waters, Australia. *Journal of Geophysical Research*, 114, 1–24.
- Boss, E., & Roesler, C. (2006). Chapter 8: Over constrained linear matrix inversion with statistical selection. In V. Stuart (Ed.), *Remote sensing of inherent optical properties: fundamentals, tests of algorithms, and applications* (pp. 57–62). Dartmouth, CA: IOCCG.
- Bowers, D. G., & Binding, C. E. (2006). The optical properties of mineral suspended particles: A review and synthesis. *Estuarine, Coastal and Shelf Science*, 67, 219–230.
- Bowers, D. G., Harker, G. E. L., & Stephan, B. (1996). Absorption spectra of inorganic particles in the Irish Sea and their relevance to remote sensing of chlorophyll. *International Journal of Remote Sensing*, 17, 2449–2460.
- Brando, V. E., Dekker, A. G., Park, Y. J., & Schroeder, T. (2012). An adaptive semi-analytical inversion of ocean colour radiometry in optically complex waters. *Applied Optics*, 51, 2808–2833.
- Brewin, R. J., Devred, E., Sathyendranath, S., Lavender, S., & Hardman-Mountford, N. J. (2011). Model of phytoplankton absorption based on three class sizes. *Applied Optics*, 50, 4535–4549.
- Bricaud, A., Babin, M., Morel, A., & Claustre, H. (1995). Variability in the chlorophyll-specific absorption-coefficients of natural phytoplankton - analysis and parameterization. *Journal of Geophysical Research-Oceans*, 100, 13321–13332.
- Buiteveld, H., Hakvoort, J. H., & Donze, M. (1994). Optical properties of pure water. In J. S. Jaffe (Ed.), *Ocean Optics XVII* (pp. 174–183): SPIE.
- Carder, K. L., Cannizzaro, J. P., Chen, R., & Lee, Z. P. (2006). Chapter 9: MODIS Semi-analytic algorithm for IOP. In V. Stuart (Ed.), *Remote sensing of inherent optical properties: fundamentals, tests of algorithms, and applications* (pp. 63–71). Dartmouth, CA: IOCCG.
- Carder, K. L., Chen, F. R., Lee, Z. P., Hawes, S. K., & Kamykowski, D. (1999). Semianalytic Moderate-Resolution Imaging Spectrometer algorithms for chlorophyll a and absorption with bio-optical domains based on nitrate-depletion temperatures. *Journal of Geophysical Research-Oceans*, 104, 5403–5421.
- Chang, G. C., Barnard, A. H., & Zanefeld, J. R. V. (2007). Optical closure in a complex coastal environment: particle effects. *Applied Optics*, 46, 7679–7692.
- Chang, G. C., Mahony, K., Briggs-Whitmitte, A., Kohler, D. D. R., Mobley, C. D., Lewis, M. R., et al. (2004). The new age of hyperspectral oceanography. *Oceanography*, 17, 16–23.
- Ciotti, A. M., Lewis, M. R., & Cullen, J. J. (2002). Assessment of the relationships between dominant cell size in natural phytoplankton communities and the spectral shape of the absorption coefficient. *Limnology and Oceanography*, 47, 404–417.
- CTDEP (2005). *Monitoring phytoplankton community composition in Long Island Sound with HPLC photopigment profiles*. Hartford, CT: Connecticut Department of Environmental Protection.
- Dekker, A. G., Vos, R. J., & Peters, S. W. M. (2001). Comparison of remote sensing data, model results and in situ data for total suspended matter (TSM) in the southern Frisian lakes. *Science of the Total Environment*, 268, 197–214.
- Dekker, A. G., Vos, R. J., & Peters, S. W. M. (2002). Analytical algorithms for lake water TSM estimation for retrospective analyses of TM and SPOT sensor data. *International Journal of Remote Sensing*, 23, 15–35.
- Dierssen, H. M. (2010). Perspectives on empirical approaches for ocean color remote sensing of chlorophyll in a changing climate. *Proceedings of the National Academy of Sciences*, 107, 17073–17078.
- Dierssen, H. M., Kudela, R. M., Ryan, J. P., & Zimmerman, R. C. (2006). Red and black tides: Quantitative analysis of water-leaving radiance and perceived color for phytoplankton, color dissolved organic matter, and suspended sediments. *Limnology and Oceanography*, 51, 2646–2659.
- Doerffer, R., & Schiller, H. (2007). The MERIS Case 2 water algorithm. *International Journal of Remote Sensing*, 28, 517–535.
- Fargion, G. S., & Mueller, J. L. (2000). Ocean optics protocols for satellite ocean color sensor validation, Revision 2. In G.S.F.S. Center (Ed.), Greenbelt, MA: National Aeronautics and Space Administration.
- Feng, H., Campbell, J. W., Dowell, M. D., & Moore, T. S. (2005). Modeling spectral reflectance of optically complex waters using bio-optical measurements from Tokyo Bay. *Remote Sensing of Environment*, 99, 232–243.
- Fournier, G. R., & Forand, J. L. (1994). Analytic phase function for ocean water. In J. S. Jaffe (Ed.), *Ocean Optics XII, Proc. SPIE*, 2258. (pp. 194–201).
- Garver, S. A., & Siegel, D. A. (1997). Inherent optical property inversion of ocean color spectra and its biogeochemical interpretation. 1. Time series from the Sargasso Sea. *Journal of Geophysical Research-Oceans*, 102, 18607–18625.
- Gilerson, A., Zhou, J., Hlaing, S., Ioannou, I., Gross, B., Moshary, F., et al. (2008). Fluorescence Component in the Reflectance Spectra from Coastal Waters. II. Performance of retrieval algorithms. *Optics Express*, 16, 2446–2460.
- Gleason, A. C. R., Voss, K. J., Gordon, H. R., Twardowski, M., Sullivan, J., Trees, C., et al. (2012). Detailed validation of the bidirectional effect in various Case I and Case II waters. *Optics Express*, 20, 7630–7645.
- Gordon, H. R., Brown, O. B., Evans, R. H., Brown, J. W., Smith, R. C., Baker, K. S., et al. (1988). A semi-analytic radiance model of ocean color. *Journal of Geophysical Research*, 93, 10909–10924.
- Gordon, H. R., Brown, O. B., & Jacobs, M. M. (1975). Computed relationships between the inherent and apparent optical properties of a flat homogenous ocean. *Applied Optics*, 14, 417–427.
- Gordon, H. R., & Morel, A. (1983). *Remote sensing of ocean color for interpretation of satellite visible imagery: A review*. New York: Springer-Verlag.
- Gould, R. W., Arnone, R. A., & Sydor, M. (2001). Absorption, scattering; and remote-sensing reflectance relationships in coastal waters: Testing a new inversion algorithm. *Journal of Coastal Research*, 17, 328–341.
- Hlaing, S., Gilerson, A., Harmel, T., Tonizzo, A., Weidemann, A., Arnone, R., et al. (2012). Assessment of a bidirectional reflectance distribution correction of above-water and satellite water-leaving radiance in coastal waters. *Applied Optics*, 51, 220–237.
- Hoepffner, N., & Sathyendranath, S. (1993). Determination of the major groups of phytoplankton pigments from the absorption spectra of total particulate matter. *Journal of Geophysical Research*, 98, 22,789–22,803.
- Hooker, S. B., Firestone, E. R., & Acker, J. G. (1995). Ocean optics protocols for SeaWiFS validation. In J. L. Mueller, & R. W. Austin (Eds.), *SeaWiFS Technical Report Series*. Greenbelt, MD: National Aeronautics and Space Administration.
- Hooker, S. B., Van Heukelman, L., Thomas, C., Claustre, H., Ras, J., Barlow, R., et al. (2005). *The second SeaWiFS HPLC analysis round-robin experiment (SeaHARRE-2)*. Greenbelt, MA: National Aeronautics and Space Administration, Goddard Space Flight Center.
- Ioannou, I., Gilerson, A., Gross, G., Moshary, F., & Ahmed, S. (2011). Neural network approach to retrieve the inherent optical properties of the ocean from observations of MODIS. *Applied Optics*, 50, 3168–3186.
- Johnsen, G., Samset, O., Granskog, L., & Sakshaug, E. (1994). In vivo absorption characteristics in 10 classes of bloom forming phytoplankton: taxonomic characteristics and responses to photoadaptation by means of discrimination and HPLC analysis. *Marine Ecology Progress Series*, 105, 149–157.
- Kirk, J. T. O. (1994). *Light and Photosynthesis in Aquatic Ecosystems* (2nd ed.). New York, NY: Cambridge University Press.
- Kostadinov, T. S., Siegel, D. A., Maritorena, S., & Guillocheau, N. (2007). Ocean color observations and modeling for an optically complex site: Santa Barbara Channel, California, USA. *Journal of Geophysical Research*, 112.
- Laws, E. A. (1997). *Mathematical methods for oceanographers: An introduction*. New York: John Wiley and Sons.
- Le, C. F., Li, Y. M., Zha, Y., Sun, D., & Yin, B. (2009). Validation of a quasi-analytical algorithm for highly turbid eutrophic water of Meilang Bay in Taihu Lake, China. *IEEE Transactions on Geoscience and Remote Sensing*, 47.
- Lee, Z., Arnone, R., Hu, C., Werdell, P. J., & Lubac, B. (2010). Uncertainties of optical parameters and their propagations in an analytical ocean color inversion algorithm. *Applied Optics*, 49.
- Lee, Z. P., & Carder, K. L. (2002). Effect of spectral band numbers on the retrieval of water column and bottom properties from ocean color data. *Applied Optics*, 41, 2191–2201.
- Lee, Z. P., & Carder, K. L. (2004). Absorption spectrum of phytoplankton pigments derived from hyperspectral remote-sensing reflectance. *Remote Sensing of Environment*, 89, 361–368.
- Lee, Z. P., Carder, K. L., & Arnone, R. A. (2002). Deriving inherent optical properties from water color: a multiband quasi-analytical algorithm for optically deep waters. *Applied Optics*, 41, 5755–5772.
- Lee, Z. P., Carder, K. L., & Arnone, R. (2006). Chapter 10: The quasi-analytical algorithm. In V. Stuart (Ed.), *Remote Sensing of Inherent Optical Properties: Fundamentals, Tests of Algorithms, and Applications* (pp. 73–79). Dartmouth, CA: IOCCG.
- Lee, Z., Carder, K., Arnone, R., & He, M. (2007). Determination of primary spectral bands for remote sensing of aquatic environments. *Sensors*, 7, 3428–3441.
- Lee, Z. P., Carder, K. L., Mobley, C. D., Steward, R. G., & Patch, J. S. (1999). Hyperspectral remote sensing for shallow waters: 2. Deriving bottom depths and water properties by optimization. *Applied Optics*, 38, 3831–3843.
- Lee, Z. P., Du, K., Voss, K. J., Zibordi, G., Lubac, B., Arnone, R. A., et al. (2011). An inherent-optical-property-centered approach to correct the angular effects in water-leaving radiance. *Applied Optics*, 50, 3155–3167.
- Li, Y., Olsen, C. B., Lyman, M. J., Van Heukelman, L., Wikfors, G., Miranda, L., et al. (2004). Monitoring phytoplankton in Long Island Sound with HPLC photopigment profiles. *Long Island Sound Research Conference*. State University of New York, Stony Brook, NY: Long Island Sound Foundation.
- Maritorena, S., Lee, Z., Du, K. P., Loisel, H., Doerffer, R., Roesler, C., et al. (2006). Chapter 2: Synthetic and in situ data sets for algorithm testing. In Z. Lee (Ed.), *Remote Sensing of Inherent Optical Properties: Fundamentals, Tests of Algorithms and Applications* (pp. 13–18). Dartmouth, CA: International Ocean Colour Coordinating Group.
- Maritorena, S., & Siegel, D. A. (2006). Chapter 11: The GSM semi-analytical bio-optical model. In V. Stuart (Ed.), *Remote sensing of inherent optical properties: fundamentals, tests of algorithms, and applications* (pp. 73–79). Dartmouth, CA: IOCCG.
- Maritorena, S., Siegel, D. A., & Peterson, A. R. (2002). Optimization of a semi-analytical ocean color model for global-scale applications. *Applied Optics*, 41.
- McClain, C. R. (2009). A decade of satellite ocean color observations. *Annual Review of Marine Science*, 1, 19–42.
- McKee, D., & Cunningham, A. (2005). Evidence for wavelength dependence of the scattering phase function and its implication for modeling radiance transfer in shelf seas. *Applied Optics*, 44, 126–135.
- Miller, R. L., & McKee, B. A. (2004). Using MODIS Terra 250 m imagery to map concentrations of total suspended matter in coastal waters. *Remote Sensing of Environment*, 93, 259–266.
- Mitchell, B. G., & Kiefer, D. A. (1988). Variability in pigment specific particulate fluorescence and absorption spectra in the northeastern Pacific Ocean. *Deep Sea Research*, 35, 665–689.

- Mobley, C. D. (1994). *Light and Water: Radiative Transfer in Natural Waters*. San Diego: Academic Press.
- Mobley, C. D. (1995). *Hydrolight 3.0 User's Guide*. Menlo Park, CA: SRI International.
- Morel, A., & Ahn, Y. (1990). Optical efficiency factors of free-living marine bacteria: Influence of bacterioplankton upon the optical properties and particulate organic carbon in oceanic waters. *Journal of Marine Research*, 48, 145–175.
- Morel, A., Antoine, D., & Gentili, B. (2002). Bidirectional reflectance of oceanic waters: accounting for Raman emission and varying particle scattering phase function. *Applied Optics*, 41.
- Morel, A., & Gentili, B. (1991). Diffuse reflectance of oceanic waters: its dependence on Sun angle as influenced by the molecular scattering contribution. *Applied Optics*, 30, 4427–4438.
- Morel, A., & Gentili, B. (1993). Diffuse reflectance of oceanic waters. II. Bidirectional aspects. *Applied Optics*, 32, 6864–6879.
- Morel, A., & Gentili, B. (1996). Diffuse reflectance of oceanic waters. III. Implication of bidirectionality for the remote-sensing problem. *Applied Optics*, 35, 4850–4862.
- Morel, A., & Prieur, L. (1977). Analysis of variations in ocean color. *Limnology and Oceanography*, 22, 709–722.
- Mueller, J. L. (1976). Ocean color spectra measured off the Oregon coast: characteristic vectors. *Applied Optics*, 15, 394–402.
- NRC (2011). Assessing requirements for sustained ocean color research and operations. In J. A. Yoder, D. Antoine, C. E. Del Castillo, R. H. Evans, C. Mobley, J. L. Sarmiento, S. Sathyendranath, C. F. Schueler, D. A. Siegel, & C. Wilson (Eds.). National Research Council.
- Park, Y. J., & Ruddick, K. (2005). Model of remote-sensing reflectance including bidirectional effects for case 1 and case 2 waters. *Applied Optics*, 44, 1236–1249.
- Petzold, T. J. (1972). Volume scattering functions for selected ocean waters. *Visibility Laboratory Technical Report* (pp. 72–78). San Diego, CA: Scripps Institute of Oceanography.
- Pope, R. M., & Fry, E. S. (1997). Absorption spectrum (380–700 nm) of pure water. 2. Integrating cavity measurements. *Applied Optics*, 36, 8710–8723.
- Preisendorfer, R. W. (1961). *Application of radiative transfer theory to light measurements in the sea* (pp. 11–30). Paris: International Union of Geodesy and Geophysics.
- Preisendorfer, R. W. (1965). *Radiative transfer on discrete spaces*. Oxford: Pergamon Press.
- Press, W. H., Flannery, S. A., Teukolsky, S. A., & Vetterling, W. T. (1986). *Numerical Recipes, The Art of Scientific Computing*. New York: Cambridge University Press.
- Roesler, C., & Boss, E. (2002). A novel reflectance inversion model: retrieval of beam attenuation coefficients and particle size distributions from ocean color. In S. Ackleson, & C. Trees (Eds.), *Ocean Optics XVI*: Office of Naval Research.
- Roesler, C. S., & Perry, M. J. (1995). In-situ phytoplankton absorption, fluorescence emission, and particulate backscattering spectra determined from reflectance. *Journal of Geophysical Research-Oceans*, 100, 13279–13294.
- Roesler, C. S., Perry, M. J., & Carder, K. L. (1989). Modelling in situ phytoplankton absorption from total absorption spectra in productive inland marine waters. *Limnology and Oceanography*, 34, 1510–1523.
- Ryan, J., Dierssen, H. M., Kudela, R. M., Scholin, C. A., Johnson, K. S., Chavez, F. P., et al. (2005). Coastal ocean physics and red tides: An example from Monterey Bay, California. *Oceanography*, 18, 246–255.
- Sathyendranath, S., Hoge, F. E., Platt, T., & Swift, R. N. (1993). Detection of phytoplankton pigments from ocean color: Improved algorithms. *Applied Optics*, 33, 1081–1089.
- Smith, R. C., & Baker, K. S. (1981). Optical properties of the clearest natural waters. *Applied Optics*, 20, 177–184.
- Snyder, W. A., Arnone, R., Davis, C. O., Goode, W., Gould, R. W., Ladner, S., et al. (2008). Optical scattering and backscattering by organic and inorganic particulates in U.S. coastal waters. *Applied Optics*, 47, 666–677.
- Sullivan, J. M., Twardowski, M., Zaneveld, J. R. V., Moore, C. M., Barnard, A. H., Donaghay, P. L., et al. (2006). Hyperspectral temperature and salt dependencies of absorption by water and heavy water in the 400–750 nm spectral range. *Applied Optics*, 45, 5294–5309.
- Ulloa, O., Sathyendranath, S., & Platt, T. (1994). Effect of particle size-distribution on the backscattering ratio in seawater. *Applied Optics*, 33, 7070–7077.
- Van Heukelman, L., & Thomas, C. (2001). Computer-assisted high-performance liquid chromatography method development with applications to the isolation and analysis of phytoplankton pigments. *Journal of Chromatography A*, 31–49.
- Wang, P., Boss, E. S., & Roesler, C. (2005). Uncertainties of inherent optical properties obtained from semianalytical inversions of ocean color. *Applied Optics*, 44, 4074–4085.
- Werdell, P. J., & Roesler, C. S. (2003). Remote assessment of benthic substrate composition in shallow waters using multispectral reflectance. *Limnology and Oceanography*, 48, 557–567.
- Whitmire, A. L., Boss, E., Cowles, T. J., & Pegau, W. S. (2007). Spectral variability of the particulate backscattering ratio. *Optics Express*, 15, 7019–7031.
- Wright, S. W., & Jeffrey, S. W. (2006). Pigment markers for phytoplankton production. In J. K. Volkman (Ed.), *Marine Organic Matter: Biomarkers, isotopes, and DNA* (pp. 71–104). Berlin: Springer-Verlag.
- Xiong, X., Sun, J., Barnes, W. L., & Salomonson, V. V. (2010). On-orbit calibration and performance of Aqua MODIS reflective solar bands. *IEEE Transactions on Geoscience and Remote Sensing*, 48, 535–546.
- Zaneveld, J. R. V., Barnard, A. H., & Boss, E. (2005). Theoretical derivation of the depth average of remotely sensed optical parameters. *Optics Express*, 13, 9052–9061.
- Zaneveld, J. R. V., & Kitchen, J. C. (1995). The variation in the inherent optical-properties of phytoplankton near an absorption peak as determined by various models of cell structure. *Journal of Geophysical Research-Oceans*, 100, 13309–13320.